Quantifying fire effects on debris flow runout using a morphodynamic model and stochastic surrogates

Elaine T. Spiller[1], Elaine T Spiller[2], Luke A Mcguire[3], Palak Patel[4], Abani Patra[4], and E Bruce Pitman[5]

[1]Affiliation not available
[2]Department of Mathematical and Statistical Sciences, Marquette University
[3]Department of Geosciences, University of Arizona
[4]Data Intensive Studies Center, Tufts University
[5]Department of Materials Design and Innovation, University at Buffalo

January 14, 2025

Abstract

Fire affects soil and vegetation, which in turn can promote the initiation and growth of runoff-generated debris flows in steep watersheds. Postfire hazard assessments often focus on identifying the most likely watersheds to produce debris flows, quantifying rainfall intensity-duration thresholds for debris flow initiation, and estimating the volume of potential debris flows. This work seeks to expand on such analyses and forecast downstream debris flow runout and peak flow depth. Here, we report on a high-fidelity computational framework that enables debris flow simulation over two watersheds and the downstream alluvial fan, although at significant computational cost. We then develop a Gaussian Process surrogate model, allowing for rapid prediction of simulator outputs for untested scenarios. We utilize this framework to explore model sensitivity to rainfall intensity and sediment availability as well as parameters associated with saturated hydraulic conductivity, hydraulic roughness, grain size, and sediment entrainment. Simulation results are most sensitive to and grain size. Further, we use this approach to examine variations in debris flow inundation patterns at different stages of postfire recovery. Sensitivity analysis indicates that constraining temporal changes in hydraulic roughness and grain size following fire would be particularly beneficial for forecasting debris flow runout throughout the postfire recovery period. The emulator methodology presented here also provides a means to compute the probability of a debris flow inundating a specific downstream region, consequent to a forecast or design rainstorm. This workflow could be employed in prefire scenario-based planning or postfire hazard assessments.

Quantifying fire effects on debris flow runout using a morphodynamic model and stochastic surrogates

Elaine T. Spiller[1], Luke A. McGuire[2], Palak Patel[3], Abani Patra[3], and E. Bruce Pitman[4]

[1]Department of Mathematical and Statistical Sciences, Marquette University, Milwaukee, Wisconsin, USA
[2]Department of Geosciences, University of Arizona, Tucson, Arizona, USA
[3]Data Intensive Studies Center, Tufts University, Medford, Massachusetts, USA
[4]Department of Materials Design and Innovation, University at Buffalo, Buffalo, New York, USA

Correspondence: Elaine T. Spiller (elaine.spiller@marquette.edu)

Abstract. Fire affects soil and vegetation, which in turn can promote the initiation and growth of runoff-generated debris flows in steep watersheds. Postfire hazard assessments often focus on identifying the most likely watersheds to produce debris flows, quantifying rainfall intensity-duration thresholds for debris flow initiation, and estimating the volume of potential debris flows. This work seeks to expand on such analyses and forecast downstream debris flow runout and peak flow depth. Here, we report on a high-fidelity computational framework that enables debris flow simulation over two watersheds and the downstream alluvial fan, although at significant computational cost. We then develop a Gaussian Process surrogate model, allowing for rapid prediction of simulator outputs for untested scenarios. We utilize this framework to explore model sensitivity to rainfall intensity and sediment availability as well as parameters associated with saturated hydraulic conductivity, hydraulic roughness, grain size, and sediment entrainment. Simulation results are most sensitive to and grain size. Further, we use this approach to examine variations in debris flow inundation patterns at different stages of postfire recovery. Sensitivity analysis indicates that constraining temporal changes in hydraulic roughness and grain size following fire would be particularly beneficial for forecasting debris flow runout throughout the postfire recovery period. The emulator methodology presented here also provides a means to compute the probability of a debris flow inundating a specific downstream region, consequent to a forecast or design rainstorm. This workflow could be employed in prefire scenario-based planning or postfire hazard assessments.

1 Introduction

Fire alters soil and vegetation, leading to increases in runoff and erosion McGuire et al. (2024); Moody et al. (2013). In extreme cases, particularly when steep watersheds burn at moderate or high severity, rapid entrainment of sediment into runoff can produce debris flows Kean et al. (2011); Gabet and Bookter (2008); Esposito et al. (2023); Conedera et al. (2003); Nyman et al. (2011); Diakakis et al. (2023). Postfire debris flows generated by runoff are most common in the first year following fire, when fire-driven reductions in soil infiltration capacity, rainfall interception, and hydraulic roughness are most extreme DeGraff et al. (2015); Hoch et al. (2021); Thomas et al. (2021); Esposito et al. (2023); Graber et al. (2023). Due to the complex interactions among runoff, sediment transport, and debris-flow initiation and runout following fire, mathematical models that couple these processes have the potential to inform our understanding of the magnitude and downstream effects of postfire debris flows, including how they change through time as landscapes recover McGuire et al. (2021). Postfire debris flows can drive sediment yields that are orders of magnitude above background rates Nyman et al. (2015) and provide an important link between hillslopes, channels, and fans in the postfire sediment cascade McGuire et al. (2024). Predictions of the size and travel distance of postfire debris flows are therefore beneficial for hazard assessments as well as our more general understanding landscape evolution in fire-prone regions Orem and Pelletier (2016); Struble et al. (2023).

The exploration of postfire debris flow processes through application of morphodynamic models for runoff and sediment transport, however, is often limited by the high dimensionality, poor constraints on parameters, and substantial computation time of the models. Quantification of uncertainties associated with sources and model parameters, and incorporation of those uncertainties in probabilistic predictions of hazard, often require use of simulation ensembles with hundreds or thousands of members, greatly increasing computational costs Bayarri et al. (2015). In this work, we accelerate a recently developed

morphodynamic model of runoff and sediment transport McGuire et al. (2017), and pair model runs with stochastic surrogates for high-dimensional output Gu and Berger (2016) as a strategy for simulating the initiation, growth, and runout of postfire debris-flows. This acceleration also enables us to rapidly explore l[illegible]rainfall intensity and fire effects on soil and vegetation, including how they change with time since fire, [illegible]ence debris flow runout and inundation patterns.

The processes leading to the initiation and growth of postfire runoff-generated debris flows involve the generation of spatially distributed overland flow and its subsequent interaction with sediment on hillslopes and in channels Santi et al. (2008); Staley et al. (2014); McGuire et al. (2017); Guilinger et al. (2020). This presents a contrast to debris flows that mobilize from shallow landslides, which initiate when infiltration promotes increases in pore-water pressure that causes a discrete mass of soil to become unstable on a hillslope Iverson et al. (1997). The source of sediment for postfire runoff-generated debris flows can come from a combination of processes, including widespread, shallow erosion on hillslopes in response to raindrop-driven sediment transport and unconfined sheet flow, rill erosion on hillslopes in areas of concentrated flow, and channel scour Santi et al. (2008); Staley et al. (2014); McGuire et al. (2017); Tang et al. (2019). All three processes are more efficient at eroding sediment following fire as a result of decreases in ground cover and increases in runoff Robichaud et al. (2016), particularly rill and channel erosion processes where overland flow does the work to entrain and transport sediment Sheridan et al. (2007); Wagenbrenner et al. (2010). In areas of unconfined, shallow flow, raindrops facilitate sediment detachment and transport in combination with runoff Kinnell (2005). Raindrop-driven sediment transport on hillslopes increases following fire due to removal of the vegetation canopy, litter, and duff, that tend to shield the soil surface from raindrop impact in unburned settings.

Models designed to simulate runoff-generated debris flows from initiation to deposition must therefore account for spatially distributed runoff and sediment transport as well as changes in flow behavior resulting from spatial and temporal variations in sediment concentration. Fully developed debris flows are characterized by volumetric sediment concentrations in excess of 40-50%, though they initiate from runoff with initially negligible sediment concentration. Postfire runoff-generated debris flows initiate in response to short-duration bursts of high intensity rainfall Kean et al. (2011). Rainfall intensity averaged over a 15-minute time period, I_{15}, is correlated well with runoff magnitude at the outlet of small, recently burned watersheds. Moreover, threshold values of I_{15} have proven to be reasonable predictors for debris flow initiation in the western USA Kean et al. (2011); Staley et al. (2017). Rainstorms that contain multiple, distinct bursts of high intensity rainfall, such as where I_{15} exceeds the debris flow threshold multiple times in a single event, can lead to multiple pulses of debris flow activity Kean et al. (2011). One benefit of morphodynamic models that are capable of simulating the debris-flow lifecycle from initiation to runout is their ability to directly account for the effects of temporally varying rainfall intensity on debris flow processes, including the formation of distinct debris flow surges and their influence on inundation extent. In contrast, models designed only to simulate debris flow runout processes (i.e. neglecting runoff and sediment transport), can be employed by defining an inflow hydrograph above the anticipated runout zone based on a runoff hydrograph and an estimated debris flow volume, or by allowing a pile of sediment and water to flow downstream from a pre-defined initiation zone Barnhart et al. (2021); Gorr et al. (2022); Gibson et al. (2022). As a result, employing morphodynamic models to estimate debris flow runout avoids introducing epistemic uncertainty associated with specifying a volume of material associated with an inflow hydrograph.

McGuire et al. 2017 developed a model that accounts for infiltration, runoff, sediment transport, and changes to flow resistance driven by sediment concentration in order to simulate postfire debris flow initiation and growth. In this model, rainfall drives sediment entrainment and transport processes that naturally lead to debris flow initiation when hydrogeomorphic conditions give rise to flows with sufficiently high sediment concentrations. Since rainfall, runoff, and erosion processes are related to model parameters known to change following fire, such as saturated hydraulic conductivity Perkins et al. (2022); Ebel et al. (2022); Thomas et al. (2021), hydraulic roughness Stoof et al. (2015), and vegetation cover Stoof et al. (2012), this framework can be used to explore how postfire recovery affects debris-flow initiation, growth, and runout. The model is computationally intensive, especially when simulating debris flow initiation and runout processes over large areas, and contains a number of parameters that are challenging to constrain McGuire et al. (2016, 2017). Thus far, model applications have been limited to examining debris-flow initiation processes in small headwater basins ($< 0.2\ \mathrm{km}^2$) where prior work and intensive field monitoring helped constrain parameter values McGuire et al. (2021, 2017); Tang et al. (2019). Here, we employ adaptive mesh refinement and parallel computations through the Titan framework Patra et al. (2005); Dalbey et al. (2008) to make model application more tractable over larger spatial domains, specifically with the goal of simulating the entirety of the postfire debris-flow lifecycle from runoff generation and debris flow growth to runout. In addition, we employ statistical emulators trained on well-chosen simulation ensembles, for fast approximations to solutions of the model equations, to explore the influence of model parameters on debris-flow runout extent and the temporal persistence of debris flow hazards after fire.

Gaussian process emulators (GPs) are a powerful class of statistical surrogates that enable rapid approximation and uncertainty quantification of computationally intensive first principles (conservation laws) based models or, *simulators* Currin et al. (1988); Sacks et al. (1989b); Welch et al. (1992). In the context of postfire debris-flows, GPs offer a mechanism to quickly explore spatial patterns in peak flow depth and area inundated for various parameter settings. GPs also allow for uncertainty quantification via Monte Carlo (MC) simulations of flow inundation. Along the way, GPs offer an approximate sensitivity analysis of physical parameters' effects on debris-flow inundation. Parallel partial emulation (PPE) Gu and Berger (2016) extends the GP methodology to field-valued outputs – in our case, flow depth at each map point (pixel). Some recent studies use PPE for flow model sensitivity analysis and calibration Zhao et al. (2021); Zhao and Kowalski (2022). In this work, we apply PPE to explore the effects of rainfall intensity and sediment availability as well as parameters associated with saturated hydraulic conductivity, hydraulic roughness, grain size, and sediment entrainment on peak debris flow depth and inundation extent.

2 Study Area

The Thomas Fire ignited in December 2017 and burned more than 1100 km^2, including a series of steep watersheds in the Santa Ynez Mountains above the community of Montecito, USA (Figure 1a). On 9 January 2018, widespread rainfall developed over the burned area in association with an atmospheric river Oakley et al. (2018). A narrow cold frontal rainband (NCFR), a relatively small-scale feature characterized by a band of intense precipitation that forms along a cold front, moved over burned watersheds above Montecito and produced a short-duration burst of intense rainfall. Peak 15-minute rainfall intensities, I_{15}, in this area ranged from approximately $78\ \mathrm{mm\ h^{-1}}$ to $105\ \mathrm{mm\ h^{-1}}$ Kean et al. (2019). During this time period, rainfall intensities

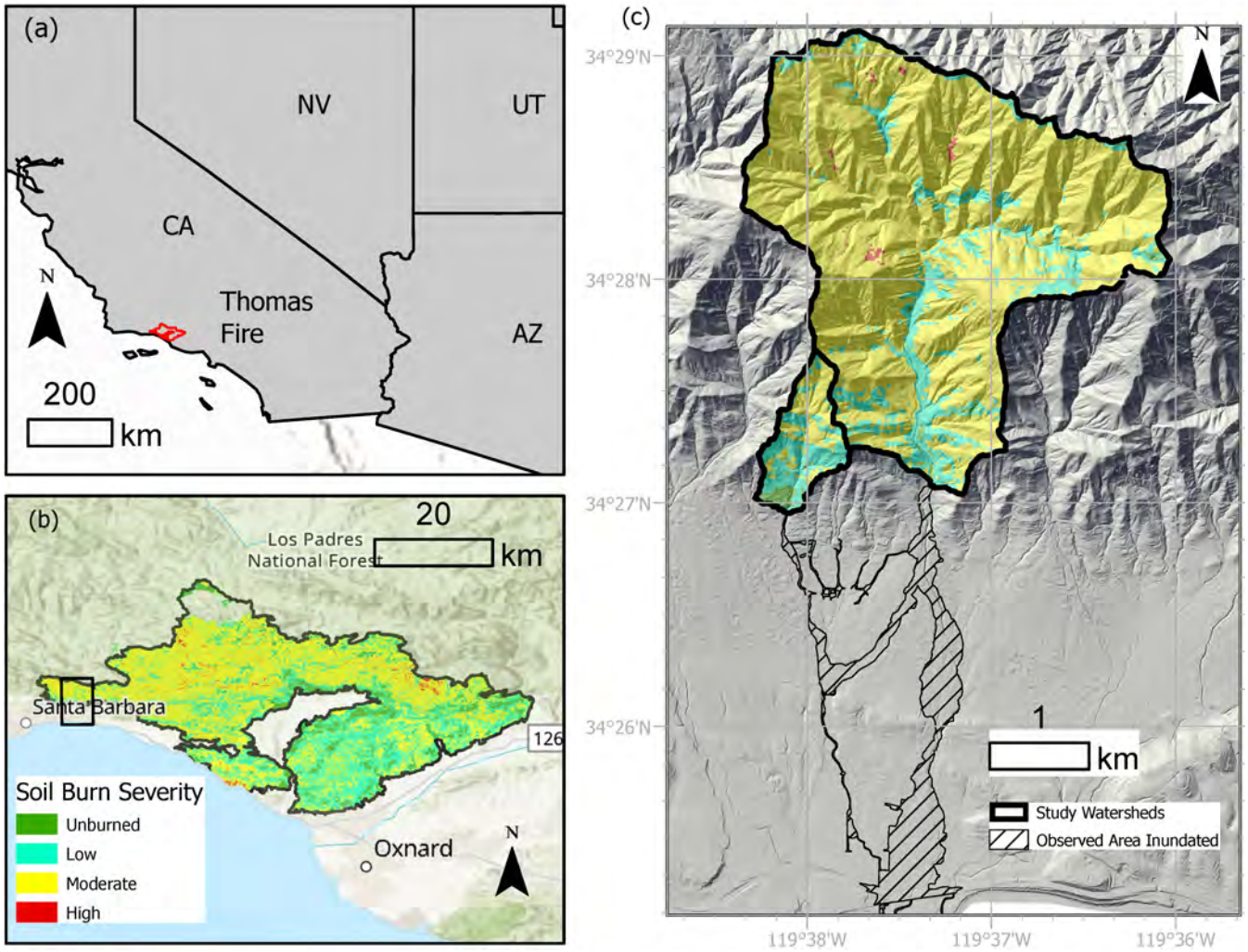

Figure 1. (a) The Thomas Fire ignited on 4 December 2017 and burned over 1140 km^2 in southern California, USA. (b) The western portion of the burned area included a series of steep watersheds (black rectangle) above the community of Montecito, located near Santa Barbara. (c) Our study focuses on two watersheds, Oak Creek (0.45 km^2) and San Ysidro Creek (7.6 km^2), located upstream of Montecito.

greatly exceeded the infiltration capacity of the soil, leading to infiltration-excess overland flow that generated rills on steep hillslopes Alessio et al. (2021). The combination of intense hillslope erosion and channel incision led to runoff-generated debris flows that traveled across the populated alluvial fan Kean et al. (2019); Morell et al. (2021); Alessio et al. (2021). The debris flows that initiated in six watersheds above Montecito mobilized more than 630,000 m^3 of sediment and led to 23 fatalities, 408 damaged structures, and more than $1 billion in damage Kean et al. (2019); Lancaster et al. (2021). In this study, we focus on modeling debris flow initiation, growth, and runout for two of these watersheds, Oak Creek and San Ysidro Creek. These watersheds are well suited for our study since high resolution topographic and rainfall data are available and we can

leverage data collection following the fire Kean et al. (2019) and previous work in the Transverse Ranges of southern California McGuire et al. (2016, 2021); Tang et al. (2019); McGuire et al. (2017) to constrain model parameter ranges. In addition, the model domain, which includes the watersheds and downstream alluvial fan, is large enough to make physics-based simulations computationally challenging (Figure 1c).

Roughly 85% of San Ysidro Creek, which has a total drainage area of $7.6\ \mathrm{km}^2$, burned at moderate or high severity (Figure 1c). Approximately 49% of Oak Creek, which is substantially smaller at $0.45\ \mathrm{km}^2$, burned at moderate or high severity. Both the San Ysidro and Oak Creek watersheds are steep, with median slopes of 28 and 21 degrees, respectively. The debris flows that initiated in San Ysidro Creek and Oak Creek mobilized a total volume of 307,000 m^3 and inundated an area of 1,007,000 m^2 Kean et al. (2019) (Figure 1c). The grain size distribution in the debris flows was bimodal, consisting of a sandy matrix that suspended boulders with a large axis greater than several meters Kean et al. (2019). Sediment from burned hillslopes likely supplied a substantial fraction of the sediment contained in the debris-flow matrix, which had a median grain diameter of approximately $0.1 - 0.3\ \mathrm{mm}$ Kean et al. (2019).

3 Methodology

3.1 Simulating runoff-generated debris flows with Titan2D

Steep watersheds recently burned by fire often experience greater amounts of runoff and increased rates of sediment transport. Factors affecting rates of sediment transport, and also the initiation and growth of runoff-generated debris flows, include rainfall intensity and duration, vegetation cover, soil infiltration capacity, and sediment characteristics (e.g. grain size, erodibility). The model developed by McGuire et al. 2017 represents rainfall, infiltration, fluid flow, and sediment entrainment and deposition processes, which makes it a useful framework for simulating runoff-generated debris flows in steep terrain McGuire et al. (2017); Tang et al. (2020). The model couples fluid flow, entrainment and deposition processes, and topographic change, such that the topography can evolve during a rainstorm in response to flow. We provide a brief overview of the governing equations, which we solve within the Titan2D framework Patra et al. (2005); Simakov et al. (2019).

The Titan2D code employs an adaptive mesh, finite volume scheme to solve hyperbolic PDEs describing shallow-water like mass flows over digital elevation models of real topography. Titan2D Patra et al. (2005) was originally developed to solve the depth averaged shallow-water mass flow equations by Savage and Hutter (1989). Titan was modernized and restructured in 2019 Simakov et al. (2019) to optimize storage and access for parallel adaptive mesh refinement, and to facilitate the usage of new material models. Using Titan2D to solve the model equations proposed by McGuire et al. 2017 therefore offers several advantages, especially for simulating debris flows over spatial scales of more than a few square kilometers. In particular, Titan2D uses *partitioned hash-tables* for better memory allocation structures, allowing it to compute over a large domain employing adaptive mesh refinement (AMR) and unrefinement, with computational efficiency. It is also well suited for parallel computing using MPI and OpenMP and dynamic load balancing for exploiting multiprocessor computing. The computational efficiencies attained make it tractable to simulate end-to-end flows from initiation to inundation and/or run the ensembles needed to train GPs efficiently.

The equations representing the motion of fluid and sediment can be written as a set of depth averaged conservation laws,

$$\frac{\partial \mathbf{U}}{\partial t} + \frac{\partial \mathbf{F}}{\partial x} + \frac{\partial \mathbf{G}}{\partial y} = \mathbf{S_0} + \mathbf{S_1} + \mathbf{S_2}, \tag{1}$$

where

$$\mathbf{U} = \left\{ h \quad uh \quad vh \quad c_1 h \quad \cdots \quad c_k h \right\}^T, \tag{2}$$

$$\mathbf{F} = \left\{ hu \quad hu^2 + \tfrac{1}{2} g_z h^2 \quad huv \quad huc_1 \quad \cdots \quad huc_k \right\}^T, \tag{3}$$

$$\mathbf{G} = \left\{ hv \quad huv \quad hv^2 + \tfrac{1}{2} g_z h^2 \quad hvc_1 \quad \cdots \quad hvc_k \right\}^T, \tag{4}$$

and where h, u, v, and c_i are flow depth, velocity along x-axis, velocity along y- axis, and sediment concentration of particle size class i. Components of gravitational acceleration in the x, y, and z directions are given by g_x, g_y, and g_z, respectively, and k denotes the number of particle size classes. $\mathbf{S_0}$, $\mathbf{S_1}$ and $\mathbf{S_2}$ are source terms. $\mathbf{S_0}$ denotes the contributions of mass sources and sinks associated with the effective rainfall rate, P_{eff}, and the soil infiltration capacity, I, as well as momentum sources and sinks arising from variations in topographic elevation, and spatial variations in sediment concentration and debris flow resistance terms, S_x and S_y. Specifically, $\mathbf{S_0}$ is given as

$$\mathbf{S_0} = \begin{Bmatrix} P_{eff} - I + \frac{\partial z}{\partial t} \\ -g_x h + \gamma_x - \psi S_x \\ -g_y h + \gamma_y - \psi S_y \\ 0 \\ \vdots \\ 0 \end{Bmatrix}. \tag{5}$$

The flow resistance terms are influenced by sediment concentration since flow behavior can change substantially as sediment concentration increases Jakob et al. (2005); Pierson and Costa (1987), though there is no universal approach for representing these changes in morphodynamic models where sediment concentration can change rapidly in space and time. Following McGuire et al. 2016, the debris flow resistance terms are scaled by ψ, which increases linearly from 0 to 1 as the volumetric sediment concentration increases from 0.2 to 0.4. This scaling factor gradually increases the importance of the debris flow resistance terms as volumetric sediment concentration approaches levels that are consistent with a transition from with flood flow to debris flow. The terms γ_x and γ_y account for the effects of spatially variable sediment concentration and are given by

$$\gamma_x = \frac{-(\rho_s - \rho_w) g_z h^2}{2\rho_f} \frac{\partial c}{\partial x} \tag{6}$$

and

$$\gamma_y = \frac{-(\rho_s - \rho_w) g_z h^2}{2\rho_f} \frac{\partial c}{\partial y} \tag{7}$$

Here, c denotes volumetric sediment concentration, $\rho_w = 1000 \text{ kg m}^{-3}$ the density of water, $\rho_s = 2600 \text{ kg m}^{-3}$ the density of sediment, and $\rho_f = c\rho_f + (1-c)\rho_w$ the density of the flow. $\mathbf{S_1}$ accounts for flow resistance using a depth-dependent Manning's

formulation, and is given as

$$\mathbf{S_1} = \begin{Bmatrix} 0 \\ g_z \eta^2 hu\sqrt{hu^2+hv^2}/h^{7/3} \\ g_z \eta^2 hv\sqrt{hu^2+hv^2}/h^{7/3} \\ 0 \\ \vdots \\ 0 \end{Bmatrix}, \tag{8}$$

where η is the Manning friction coefficient. The friction coefficient varies with flow depth according to

$$\eta = \begin{cases} \eta_0 \left(h/h_c\right)^{-\epsilon} & h \leq h_c \\ \eta_0 & h > h_c \end{cases}, \tag{9}$$

where η_0 is the hydraulic roughness coefficient, h_c is a critical flow depth and ϵ is a phenomenological exponent. Soil infiltration capacity, I, is represented by the Green-Ampt model where

$$I = k_s \frac{Z_f + h_f + h}{Z_f}, \tag{10}$$

with k_s denoting saturated hydraulic conductivity, h_f the wetting front potential, $Z_f = V/(\theta_s - \theta_i)$ the depth of the wetting front, V the cumulative infiltrated depth, θ_s the volumetric soil moisture content at saturation, and θ_i the initial volumetric soil moisture content. The source term $\mathbf{S_2}$ accounts for sediment entrainment and deposition processes, which are represented using the framework proposed Hairsine and Rose (1992a, b). In particular,

$$\mathbf{S_2} = \begin{Bmatrix} 0 \\ 0 \\ 0 \\ e_1 + e_{r1} + r_1 + r_{r1} - d_1 \\ \vdots \\ e_k + e_{rk} + r_k + r_{rk} - d_k \end{Bmatrix}, \tag{11}$$

where e_k and e_{rk} are sediment detachment and re-detachment rates due to raindrop impact for sediment particles in size class k, r_k and r_{rk} are rates of entrainment and re-entrainment due to runoff, and d_k is the effective deposition rate. The model differentiates between original soil, which has not yet been entrained and transported during the modeled rainstorm, and deposited sediment, which has been detached and subsequently deposited. Detachment rates for entraining original sediment and re-entraining deposited sediment are computed differently. Sediment in the deposited layer can also fail en-masse McGuire et al. (2017). Rates of sediment entrainment and re-entrainment by runoff are given by

$$r_k = (1 - H) p_k \frac{F(\Omega - \Omega_{cr})}{J}, \tag{12}$$

and

$$r_{rk} = H\frac{m_k}{m_t}\frac{F(\Omega-\Omega_{cr})}{\frac{\rho_s-\rho_f}{\rho_s}gh}. \tag{13}$$

Here, m_k is the deposited sediment mass per unit area for sediment in size class k, m_t is the total mass of deposited sediment per unit area, $H = \min(m_t/m_t^*, 1)$ accounts for the degree to which deposited sediment shields the underlying bed from erosion, m_t^* is the mass of deposited sediment needed to completely shield original sediment from erosion, ρ_f is the density of the flow, ρ_s is the density of sediment, F denotes the fraction of stream power effective in sediment entrainment, $\Omega = \rho_f g S_f \sqrt{uh^2+vh^2}$ is stream power, and $S_f = \eta^2(uh^2+vh^2)h^{-10/3}$ is the friction slope. In this work, we consider a single particle size class characterized by a representative particle diameter, δ.

The topographic surface evolves in response to sediment entertainment and deposition according to

$$\frac{\partial z}{\partial t} = \frac{1}{\rho_s(1-\phi)}\left(\sum_{k=1}^{K} d_k - e_k - e_{rk} - r_k - r_{rk}\right). \tag{14}$$

Here, $\phi = 0.4$ is the bed sediment porosity and e_k and e_{rk} denote the sediment detachment and redatchment rates due to raindrop impact as defined by McGuire et al. 2016. Since the equations for fluid flow and evolution of the topographic surface are coupled, the model captures feedback between erosion and flow behavior even during individual rainstorms. For example, concentration of flow in one area can lead to erosion, which promotes increased flow concentration and enhanced sediment transport.

3.2 Rainfall and model parameters

A digital elevation model (DEM) of the study area is input to the Titan2D simulation. Here, we use a 1 m DEM derived from post-event airborne lidar. Elevations and slopes at locations required by the computational mesh are obtained using a 9 point (3×3) finite difference stencil to interpolate on the DEM grid reducing the effects of artifacts and noise in the data Patra et al. (2005). Effects of uncertainty in the DEM could be propagated through the simulation and subsequent analysis Stefanescu et al. (2012b, a), but we did not consider this in the present study.

Runoff and debris flows initiated in the study area in response to a short duration, high intensity burst of rainfall in the early morning hours of 9 January 2018 Kean et al. (2019). All simulations use 1-minute rainfall intensity data derived from the KTYD rain gauge for a 20-minute time period that spans this short temporal window when rainfall intensity rapidly increased and debris flows initiated (Figure S1). The gauge is maintained by the Santa Barbara County Flood Control District and is located approximately 5 km west of the San Ysidro Creek watershed.

Simulations were designed to explore the extent to which inundated area and peak flow depths on the alluvial fan were influenced by rainfall intensity as well as several parameters that can play critical roles in debris-flow initiation and growth. Selection of these parameters was determined, in part, based on common effects of fire such as the tendency for moderate and high severity fire to reduce soil infiltration rates Ebel (2019). The relative influence of these parameters on debris flow runout extent and peak flow depth, however, is less clear. We explored the effect of different rainfall intensities by multiplying the

observed 1-minute rainfall intensity time series by a rainfall intensity factor (RI_{fac}) that we varied from 0.4 to 1.5. We also varied the representative particle diameter, δ, from $0.05-0.3$ mm, the fraction of stream power effective in entrainment, F, from $0.01-0.06$, the hydraulic roughness coefficient, n_0, from $0.03-0.2$, and saturated hydraulic conductivity, k_s, from $5-20$ mm h^{-1}. We further enforced a maximum soil thickness, r_{max}, that varied from $0.25-1.5$ m to explore the role of sediment availability. All other parameters were fixed (Table 1, Table 2). We used a Latin hypercube sampling strategy to generate 64 different parameter sets from the ranges specified above McKay et al. (1979). Each simulation took several hours to complete on an HPC cluster using up to 16 cores on an intel Xeon Gold 6226R processor.

We focus on exploring the effects of rainfall intensity, δ, F, n_0, k_s, and soil thickness (sediment availability) since they control different aspects of the debris flow initiation and growth process and, aside from rainfall intensity, they may all be strongly affected by fire in our study area Liu et al. (2021); McGuire et al. (2021). Peak rainfall intensity over sub-hourly durations, particularly the 15-minute duration, is correlated well with runoff in recently burned watersheds in southern California Kean et al. (2011). Peak 15-minute rainfall intensity is also used in empirical models designed to predict postfire debris-flow likelihood and volume in the western USA Staley et al. (2017); Gartner et al. (2014). We therefore expect that variations in rainfall intensity during the relatively short ($<$ 0.5 hours) portion of the rainstorm that we are modeling will influence debris flow processes.

We expect the representative grain size, δ, to be relatively small in areas of concentrated flow immediately following fire in our study area given the propensity for postfire dry ravel to transport hillslope sediment to channels and valley bottoms Florsheim et al. (1991); Lamb et al. (2011). Both δ and the amount of sediment available for transport, which we vary by enforcing a maximum soil thickness (r_{max}) throughout the model domain, may vary as a function of time since fire as sediment is exported from postfire rainstorms Tang et al. (2019). Similarly, Liu et al. 2021 found that k_s and the Manning coefficient were lowest during rainstorms in the first year following a high severity fire in the San Gabriel Mountains, southern California, and increased by factors of roughly 3-4 over the following 4 years. Immediately after fire in southern California, values for the Manning coefficient and saturated hydraulic conductivity can be as low as $0.025-0.07$ s $m^{-1/3}$ and $1-6$ mm h^{-1}, respectively Rengers et al. (2016); Tang et al. (2019); Liu et al. (2021). Kean et al. 2019 used post-event, point scale measurements with a tension infiltrometer to estimate the geometric mean of saturated hydraulic conductivity at 20 mm h^{-1} in the days following the Montecito debris flows. The effective fraction of stream power, F, may be expected to increase immediately following fire due to reductions in roughness associated with ground cover and vegetation. Values of $F \approx 0.005$ have performed reasonably well at reproducing past events in steep, recently burned watersheds in southern California McGuire et al. (2017); Tang et al. (2019). Soil cohesion, particle size distribution, and ground cover, among other factors, are likely to influence F and could lead to considerable site-to-site variability.

3.3 Assessing runout model performance

We assessed the ability of the model to reproduce the observed inundation extent (Figure 1) by computing a similarity index Heiser et al. (2017). The similarity index, Ω is defined according to

$$\Omega = \alpha + \beta + \gamma \tag{15}$$

where α denotes the area of overlap between simulated and observed inundation, β denotes the area where the model underestimates inundation extent, and γ the area where the model overestimates inundation extent. The similarity index varies between -1 and 1, with a greater value indicating a better fit between the model and observation.

3.4 Emulating debris flows

Statistical emulators are effectively probabilistic models of computationally intensive physical model systems or *simulators*. Statistical emulators relate a set of user-defined inputs, often physical parameter specifications, to simulator output. Gaussian process emulators (GPs) are a popular class of surrogates for approximating and quantifying uncertainties in simulators as they (almost) interpolate model output Sacks et al. (1989a, b); Santner et al. (2003); Rasmussen and Williams (2006). Further, the variance of the associated GP offers a quick mechanism to assess the uncertainty of using the emulator in place of the simulator for model prediction at untested inputs. Thus GP emulators offer a rapid and quantifiable mechanism to approximate output from physical process models that are computationally intensive to exercise. The parallel partial emulator (PPE) Gu and Berger (2016) extends this surrogate model to field-valued output.

Inputs to GP emulators are user defined. They are typically influential parameters, which show up within the governing dynamics, the forcing terms, or boundary conditions, as opposed to independent variables in the physical model. For the model described in Sec 3.1, we choose $p = 6$ parameters to define our input vector, namely those described in Sec 3.2 and given by $\mathbf{q} = [k_s, r_{max}, \eta_0, F, \delta, RI_{\text{fac}}]$. We will discuss the relationship between GP emulators and sensitivity analysis further in Sec 4.

The output under consideration, $\mathbf{y}$, is the maximum (over time) flow depth at each of $s = 2.4M$ map points. The main objective of the emulator is to predict the output of the Titan2D model at an untested scenario, $\mathbf{q}^*$, given a relatively modest set of N training or *design* runs $\mathbf{q}^{\text{D}}$ and each of their corresponding inundation depth outputs, $\mathbf{y}_j^{\text{D}}$, $j = 1, \ldots, N$. In this work, we take $N = 64$ training runs and each output, $\mathbf{y}_j^{\text{D}}$, is a $2.4M$ element vector recording the peak flow depth (inundation depth) at each map point. Collecting these outputs together, we have Y^{D}, as a $64 \times 2.4M$ matrix of training run outputs. The 64 training run inputs are chosen by a Latin hypercube design McKay et al. (1979); Santner et al. (2003) covering the ranges of inputs listed in Table 1. All other parameters are fixed (Table 2). To fit the emulator, these parameter ranges are normalized to a unit hypercube.

Given the training data, $\{\mathbf{q}^{\text{D}}, Y^{\text{D}}\}$, to approximate the inundation resulting from an untested scenario, $\mathbf{q}^*$, we use the predictive mean of the PPE given by

$$\tilde{\mathbf{y}}(\mathbf{q}^*) = \mathbf{h}^{\text{T}}(\mathbf{q}^*)B + \mathbf{r}^{\text{T}}(\mathbf{q}^*)R^{-1}(Y^{\text{D}} - H^{\text{D}}B), \tag{16}$$

Model parameter	Min value	Max value	Range parameter
k_s: Saturated hydraulic conductivity ($\mathrm{mm\ h^{-1}}$)	5	20	1.3
r_{max}: Maximum soil thickness (m)	0.25	1.5	130
η_0: hydraulic roughness coefficient ($\mathrm{s\ m^{-1/3}}$)	0.03	0.2	0.48
F: Fraction of stream power effective in sediment detachment	1.0×10^{-2}	6.0×10^{-2}	0.80
δ: Effective grain size (mm)	0.05	0.30	0.58
RI_{fac}: Rainfall intensity factor	0.4	1.5	0.74

Table 1. Parameter ranges with units and GP range parameters (unit-less) for the six parameters that varied among the N=64 debris flow simulations.

where R is an $N \times N$ (64×64 in this work) matrix of correlations between pairs of design inputs, $\mathbf{r}(\mathbf{q}^*)$ is an $N \times 1$ vector of correlations between the untested input, $\mathbf{q}^*$, and each of the input scenarios in the design, $\mathbf{q}^{\mathrm{D}}$. Further, $\mathbf{h}(\mathbf{q})$ is a $l \times 1$ vector of regression variables, often taken to be constant or linear in $\mathbf{q}$ (i.e., $l = 1$ for constant case used in this work and $l = p + 1$ for the linear case), and H^{D} is and $N \times l$ matrix where the j^{th} row are the regression variables evaluated at the j^{th} design point, $\mathbf{h}^{\mathrm{T}}(\mathbf{q}_j^{\mathrm{D}})$. The matrix B is a $l \times s$ matrix of regression coefficients. Here, each of the $s = 2.4M$ outputs has its own set of regression coefficients, but a shared correlation structure. We use a Matérn 5/2 correlation function Stein (1999). For two scenarios, e.g., two input points $\mathbf{q}_i = (x_{i1}, \ldots, x_{ip})^{\mathrm{T}}$ and $\mathbf{q}_j = (x_{j1}, \ldots, x_{jp})^{\mathrm{T}}$, the standardized distance and correlation between these input scenarios are given by

$$
\begin{aligned}
d_k &= \Big(\frac{|x_{ik} - x_{jk}|^2}{\theta_k^2} \Big)^{1/2}, \qquad k = 1, \ldots, p \\
c(\mathbf{q}_i, \mathbf{q}_j) &= \prod_{k=1}^{p} \Big(1 + \sqrt{5} d_k + \frac{5}{3} d_k^2 \Big) \exp\big(- \sqrt{5} d_k \big),
\end{aligned} \tag{17}
$$

respectively. The predictive variance for each output dimension (pixel) of the PPE is given by

$$
\begin{aligned}
\mathbf{v}_j(\mathbf{q}^*) = & \sigma_j^2 \Big(1 - \mathbf{r}^{\mathrm{T}}(\mathbf{q}^*) R^{-1} \mathbf{r}(\mathbf{q}^*) + \big(\mathbf{h}(\mathbf{q}^*) - (H^{\mathrm{D}})^{\mathrm{T}} R^{-1} \mathbf{r}(\mathbf{q}^*) \big)^{\mathrm{T}} \\
& \times \big((H^{\mathrm{D}})^{\mathrm{T}} R^{-1} H^{\mathrm{D}} \big)^{-1} \big(\mathbf{h}(\mathbf{q}^*) - (H^{\mathrm{D}})^{\mathrm{T}} R^{-1} \mathbf{r}(\mathbf{q}^*) \big) \Big),
\end{aligned} \tag{18}
$$

where σ_j^2, $(j = 1, \ldots, s)$ is the scalar variance corresponding to each pixel's output. "Fitting" a PPE amounts to estimating the regression parameters in B, the scalar variances at of each output, σ_j^2, and the *range parameters* $\{\theta_k : k = 1, \ldots, p\}$. To do so, we use the `RobustGaSP` package Gu et al. (2018, 2019). On a laptop, fitting a PPE to $2.4M$ pixels of output with $N = 64$ training runs takes roughly 10 minutes. Training the PPE scales as a cube of the number of training runs N, and linearly with the size of the simulator output, s.

GP emulators have been applied to Titan2D-based volcanic debris flows Bayarri et al. (2009, 2015); Spiller et al. (2014); Rutarindwa et al. (2019) and recently to other Titan2D-based debris flows Zhao et al. (2021); Zhao and Kowalski (2022). In

Table 2. Model parameters using the same notation as McGuire et al. 2017.

Symbol	Definition	Value	Unit
a_0	Detachability of original soil	1000	$\mathrm{kg\ m^{-2}\ s^{-1}}$
a_{d0}	Detachability of deposited sediment	2000	$\mathrm{kg\ m^{-2}\ s^{-1}}$
m^*_{t0}	Deposited sediment needed to shield original soil	2.7	$\mathrm{kg\ m^{-2}}$
J	Specific energy of entrainment	15.125	$\mathrm{m^2\ s^{-2}}$
C	Effective cohesion	200	Pa
ϕ_{bed}	Basal friction angle	32	deg
λ	Ratio of pore fluid pressure to total normal stress	0.8	-
C_v	Fraction vegetation cover	0	-
h_f	Wetting front potential	1	mm
θ_i	Initial volumetric soil moisture	0.1	-
θ_s	Volumetric soil moisture at saturation	0.39	-
ϵ	Exponent in friction model	0.33	-
h_c	Critical depth in friction model	3	mm

each of these studies, source terms (particularly debris mass or flux) were specified via ad-hoc parameterizations which are less appropriate for postfire, runoff-generated debris flows.

3.5 Numerical Experiments

Evaluation of the GP emulator's mean quickly allows one to explore any output quantity of interest over the parameter space. Here we take the output quantity of interest, $\mathbf{y}$, to be the maximum debris-flow depth at all locations. Additionally, the variance of the GP emulator accounts for the uncertainty introduced by evaluating the GP mean, $\tilde{\mathbf{y}}$, instead of the debris-flow process model. We can break our exploration of numerical experiments into four groups.

First, we perform leave-one-out experiments as a test of the PPE performance. This experiment amounts to excluding one simulation at a time, fitting a GP to the 63 remaining simulations, and then comparing the GP predicted inundation of the left-out scenario to actual simulated inundation for that scenario. This is repeated for each of the $N = 64$ simulations.

Second, we explore the relative importance of different model parameters using the GP's range parameters. The range parameters are positive numbers indicating the influence of each model parameter on the model response – the smaller the range parameter, the more influence the corresponding model parameter has on the debris flow model (i.e. maximum flow depth). As such, these range parameters act as an effective sensitivity analysis.

Third, we apply the emulator to explore how inundation extent and peak flow depths are driven by temporal changes in saturated hydraulic conductivity and hydraulic roughness that occur as the soil and land surface evolve with time after fire. This analysis is designed to illustrate how emulators can be used to efficiently quantify the temporal persistence of debris flow hazards after fire. We focus, in particular, on exploring the effects of postfire changes in saturated hydraulic conductivity and

hydraulic roughness since these two parameters are influenced by fire and Liu et al. 2021 provide guidance for parameterizing how they change with time since fire in the nearby San Gabriel Mountains. Since the GP emulator enables rapid forward uncertainty quantification, we demonstrate how it can be used to accelerate a Monte Carlo probability of inundation calculation for two cases, namely when the observed storm occurs 2 months and 14 months postfire. These discrete times for evaluating the emulator were chosen since the parameterization from Liu et al. 2021 results in substantial changes in saturated hydraulic conductivity and hydraulic roughness over the first 14 postfire months and we therefore expected to see corresponding changes in the debris flow inundation footprint.

Lastly, we explore the effect of different rainfall scenarios, as quantified by varying I_{15}, on debris flow inundation. Hazard assessments often involve quantifying the likelihood and magnitude of debris flow hazards in response to a forecast or design rainstorm. To do so here, we propose an approach that uses two different emulators to generate a probabilistic inundation map for a given value of I_{15}. One is the emulator that has already been described, which predicts peak flow depth across the landscape and is used in all of the previously described numerical experiments. The other is a second emulator that we developed specifically to facilitate this set of numerical experiments. In particular, we fit a separate GP emulator to predict the volume of sediment eroded from the upper watersheds, which we view as a proxy for the amount of sediment mobilized by debris flows. Rather than a map, the output from this GP, which we refer to as the volume emulator, is a single scalar value (e.g., $s = 1$).

Given these two emulators, the process for generating a probabilistic inundation map for a forecast or design rainstorm with a given I_{15} begins by fixing the RI_{fac} input parameter (e.g., $RI_{fac} = 0.5$ for $I_{15} = 38.5$ mm h^{-1}) and sampling all other inputs randomly over the ranges given in table 1. We then use the volume emulator to predict the total amount of sediment eroded from the upper watersheds for each sampled parameter set. We keep only those samples that lead to $\pm$ 10% of the volume predicted by the Emergency Assessment Volume model developed by Gartner et al. 2014, which is used throughout the western USA to estimate postfire debris flow volumes for an individual rainstorm with a given I_{15}. We can then take these same sets of samples that resulted in $\pm$ 10% of the target volume and evaluate the maximum flow depth GP at those parameter values. This allows us to estimate the probability of inundation, where a grid cell is considered to be inundated if the maximum flow depth is greater than or equal to 0.1 m. Involving the volume GP in this process provides a mechanism for focusing on the portion of the parameter space that leads to realistic debris flow volumes (for a given I_{15}) based on an empirical model developed for our study region. The relevant subset of the parameter space will vary with I_{15} since the Emergency Assessment Volume model predicts greater debris flow sediment volumes for greater values of I_{15}. We consider three I_{15} values in our analyses – 38.5 mm h^{-1}, 77 mm h^{-1}, and 96 mm h^{-1} – which yield debris flow sediment volumes of 88,000 m^3, 230,000 m^3, and 358,000 m^3, respectively. These values of I_{15} were chosen to be 50%, 100%, and 125% of the observed I_{15} and correspond to RI_{fac} input parameter values of 0.5, 1.0, and 1.25, respectively.

4 Results

4.1 Observed and Modeled Area Inundated

The modeled area inundated, defined as the area below the watershed outlets where flow depth exceeded 0.1 m matches the observed area inundated well within a portion of the explored parameter space. The similarity index is generally greater when the hydraulic roughness coefficient, n_0 is less than 0.1 (Figure 2). The amount of sediment eroded from the upper watersheds varies substantially from roughly 2000 m^3 to nearly $700,000$ m^3 (Figure S2, Figure 2). The observed eroded volume of $307,000$ m^3 falls near the upper range of most simulated erosion volumes (Figure 2). The similarity index generally increases with erosion volume and approaches its maximum value of roughly 0.23 where the simulated and observed erosion volumes are similar (Figure 2).

4.2 Emulator performance

We examine leave-one-out predictions to test the performance of the GP emulator for approximating the Titan2D simulations. The range parameter estimates were very stable. More specifically, we found the coefficients of variation for each of the six range parameter values to be between 0.03–0.15 indicating that the relative influence of any input to the GP was not swayed strongly by any single flow simulation. For illustrative purposes, we focus on two points of interest – one located in a channel and one on the adjacent fan surface where flow is relatively unconfined. In Figure 3 for both cases we sort the simulations by their left-out flow depths, $\mathbf{y}$, and predict each with a credible interval centered at the mean of the GP, $\tilde{y}$. We find root mean squared errors from these leave-one-out experiments of $0.16\mathrm{m}$ and $0.36\mathrm{m}$ for the locations on the fan and on the channel, respectively. Further, we see that 89% (fan location) and 94% (channel location) of the simulated depths fall within their predictive credible intervals. These numbers are slightly below the anticipated 95%, but this is likely due to the relatively small training set, and in the case of the fan location, the fact that roughly one third of the simulations resulted in no inundation, which is challenging for GP emulation Spiller et al. (2023).

4.3 Sensitivity analysis

A crucial step to fitting a GP is estimating the range parameters. Smaller range parameters indicate that the corresponding model parameter has more influence on the debris flow model output of interest (i.e. maximum flow depth). (See the leftmost column of Table 1). Modeled peak flow depth is most sensitive to the hydraulic roughness coefficient, followed by effective grain size, rainfall intensity, fraction of stream power effective in sediment detachment, and saturated hydraulic conductivity.; it is relatively insensitive to the maximum soil thickness.

4.4 Effects of rainfall intensity on runout

One will often want to use GP surrogates in a predictive mode. We use surrogates to predict how the probability of debris flow inundation varies across three different rainfall scenarios as defined by rainstorms with a peak I_{15} of 38.5 $\mathrm{mm\ h^{-1}}$

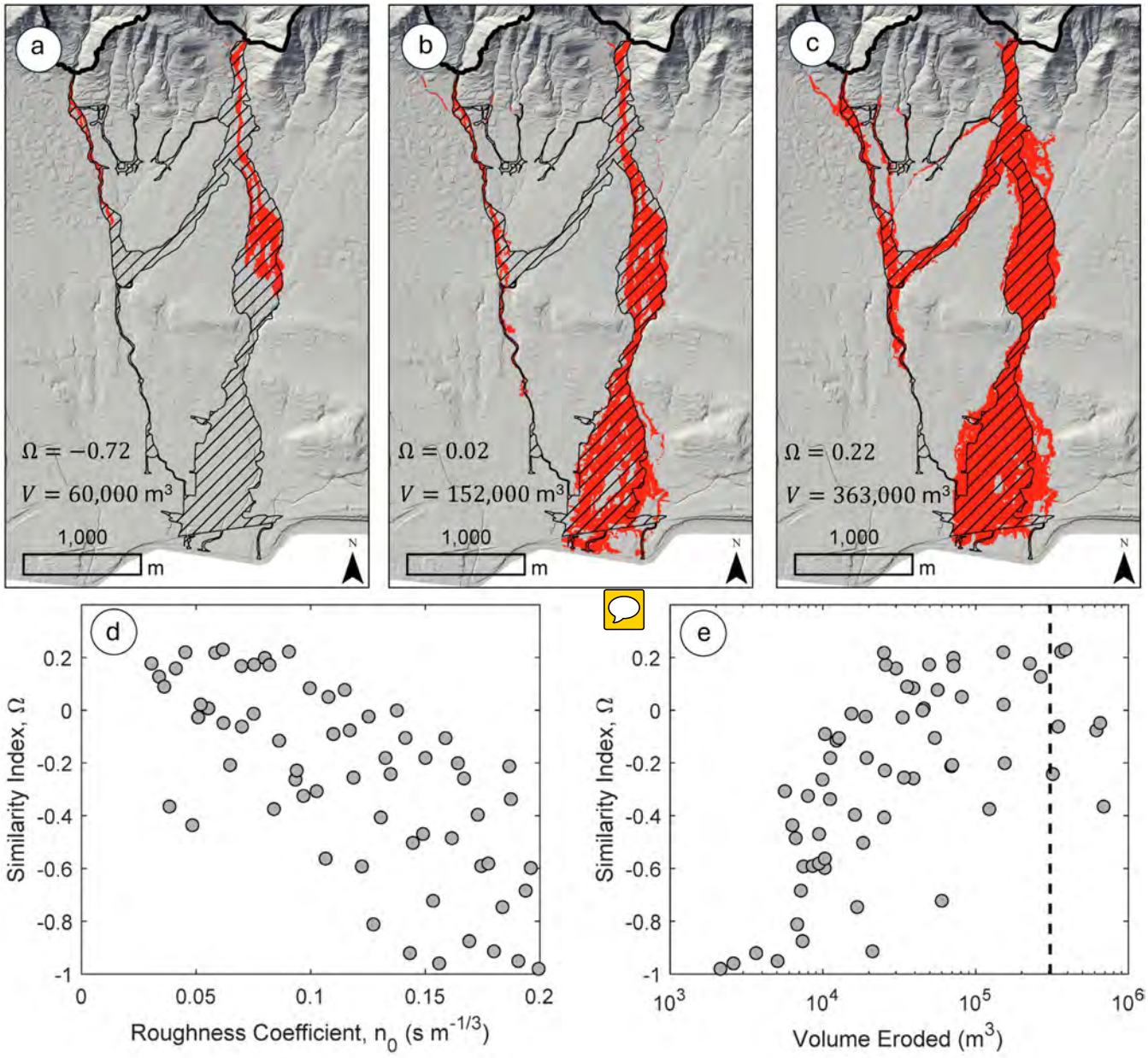

Figure 2. Comparisons between modeled and observed area inundated for flows where the volume of sediment eroded from the upper watersheds was approximately (a) $56{,}000\ \mathrm{m}^3$ (b) $153{,}000\ \mathrm{m}^3$ (c) and $356{,}000\ \mathrm{m}^3$. The observed volume of sediment eroded from the upper watersheds was $307{,}000\ \mathrm{m}^3$. (d) The similarity index, Ω, is greater, indicating a better fit between modeled and observed inundation extents, when the hydraulic roughness coefficient is low and (e) when the volume of sediment eroded from the upper watersheds is closer to the observed value (dashed black line).

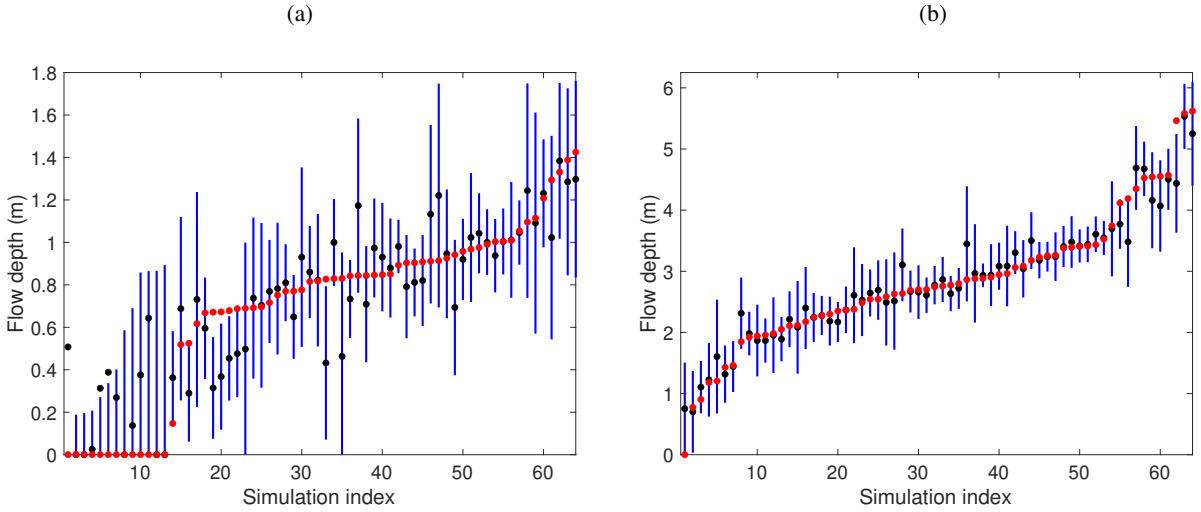

Figure 3. Leave-one-out experiments for (a) a location on the fan and (b) a location in the channel (see Figure 7 for details). In each panel, indices are sorted based on the Titan2D-simulated peak flow depth (red stars). GP predictive means for these scenarios are plotted in black while the 95% credible intervals are plotted as vertical blue bars.

($RI_{fac} = 0.5$), 77 mm h^{-1} ($RI_{fac} = 1$), and 96 mm h^{-1} ($RI_{fac} = 1.25$), respectively. Figure 4 shows scatter plots from (500 volume-targeted) samples of effective grain size (δ), effective sediment detachment fraction (F), and hydraulic roughness (η_0) against each other along with histograms of samples in each parameter. As I_{15} increases, F goes from nearly uniform to skewed toward higher values while δ values cover the whole range of grain sizes for lower I_{15}, but skew toward the smallest grain sizes for high values of I_{15}. Greater values of I_{15} are associated with greater target debris flow volumes. The observed shifts in the relevant portion of the parameter space reflect this change. For example, greater values of F and smaller values of δ produce larger debris flows (Figure S2).

Figure 5 shows a map of the probability of inundation for each rainfall scenario. The spatial footprint of area with a high probability of inundation increases substantially as I_{15} increases from 38.5 mm h^{-1} to 77 mm h^{-1}. Such a probabilistic analysis using only Titan2D simulations would be computationally challenging.

4.5 Effects of postfire recovery on runout

Liu et al. 2021 developed parametric best-fit curves to model the change in saturated hydraulic conductivity and hydraulic roughness as a function of time following fire in the nearby San Gabriel Mountains. Using these relationships, and setting others to the center of their respective ranges, we use the GP emulator to explore the effects of temporal changes in the hydraulic roughness coefficient and saturated hydraulic conductivity. Both peak flow depth and area inundated in response to the observed rainstorm would decrease substantially over the first six months following fire (Figure 6). For example, US Highway 101, which runs perpendicular to the direction of flow near the distal portion of the fan, would only be inundated

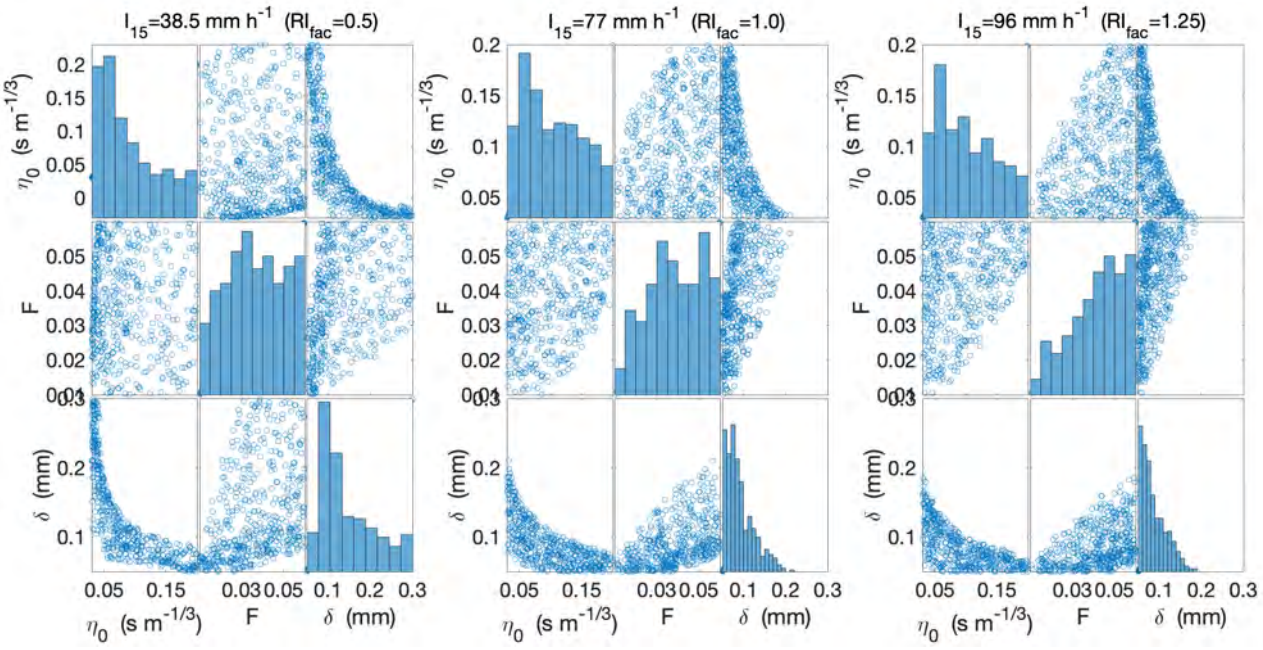

Figure 4. Left panel: $I_{15} = 38.5$ mm h^{-1} (RI_{fac}=0.5), Center panel: $I_{15} = 77$ mm h^{-1} (RI_{fac}=1), Right panel: $I_{15} = 96$ mm h^{-1} (RI_{fac}=1.5). Each panel contains histograms and pairwise scatter plots of η_0, F, and δ that result in GP volume predictions $\pm$ 10% of the targeted volumes. The target volume for a given $I15$ is defined as that predicted by the Gartner et al. 2014 Emergency Assessment Volume model. Note that the vertical and horizontal labels apply to each scatter plot in the matrix, but only the horizontal labels apply to the histograms.

when the rainstorm occurs within the first 3 months following fire. If the observed rainstorm were to have occurred 12 months following the fire, the simulated inundation area would be limited to channels near the fan apex.

We can also explore the effects of rainfall intensity and temporal changes in hydraulic roughness and saturated hydraulic conductivity following fire by examining flow depth at distinct points of interest. Again, we consider the same two points for illustrative purposes, one located in a channel and one on the adjacent fan surface where flow is relatively unconfined (Figure 7). For a given time since fire, peak flow depths are greater in the channel relative to the fan surface, as expected. Peak flow depth decreases gradually over the first several months at the point on the fan before dropping to near zero after approximately nine months. Peak flow depths decrease over the first year following fire in the channel location from roughly 4 m to 2 m. Visualizing peak flow depths as a function of time since fire and rainfall intensity can be helpful for assessing temporal shifts in the magnitude of rainfall associated with potential debris-flow impacts at different locations. For example, the area inundated by a flow in response to a rainstorm characterized by $RI_{fac} = 1$ would decrease substantially over the first 9 postfire months (Figure 6).

We further use the emulator to produce probabilistic maps of inundation at different times following fire (Figure 8). Differences in the spatial patterns of inundation likelihood are apparent between scenarios where the storm occurs 2 months following

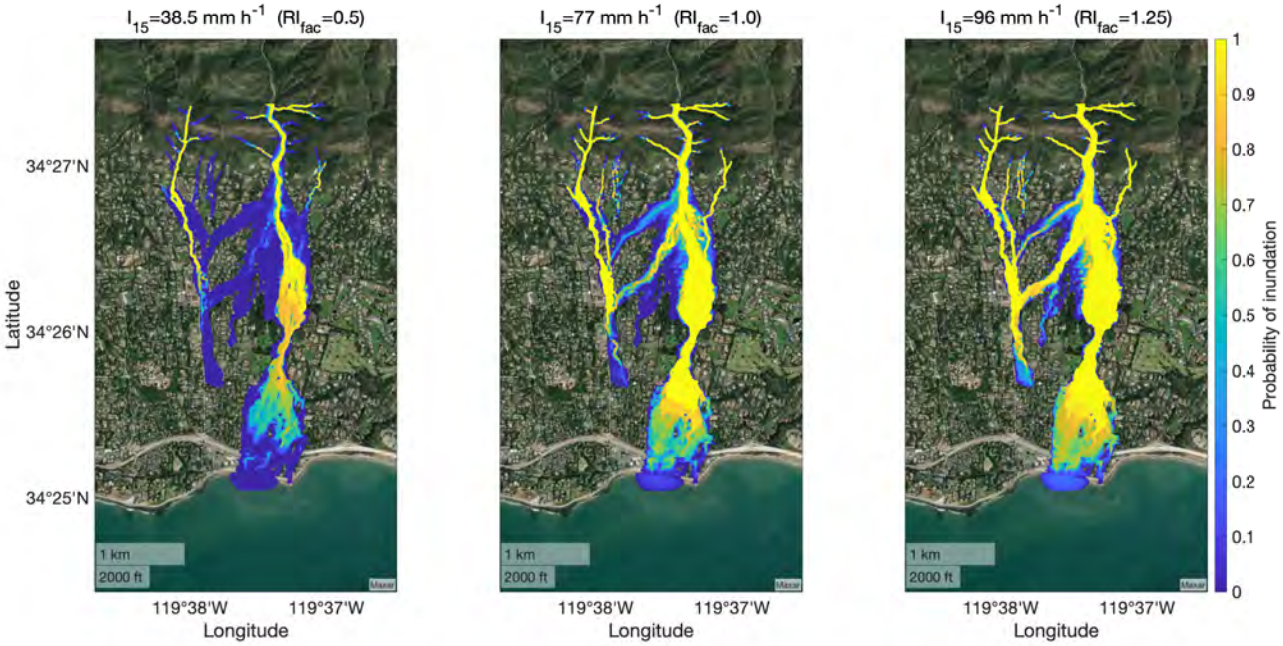

Figure 5. Probability of inundation for three rainfall scenarios: Left: $I_{15} = 38.5$ mm h^{-1} (RI_{fac}=0.5), Center: $I_{15} = 77$ mm h^{-1} (RI_{fac}=1), Right: $I_{15} = 96$ mm h^{-1} (RI_{fac}=1.5).

the fire versus 14 months. We identify a location as being inundated if peak flow depth exceeds 0.1 m. All parameters were set to their central values except for saturated hydraulic conductivity and the hydraulic roughness coefficient. The latter parameter is sampled from the distribution suggested by Liu et al. 2021 while the former is set to 2 and 14 month values, respectively, estimated from the same study. The probability MC calculation was carried out with 100 samples.

5 Discussion

5.1 Model Performance

Titan2D is able to provide reasonable estimates of inundation extent. Across the 64 Titan2D simulations, which only sparsely cover the parameter space, the maximum similarity index of 0.23 is similar to what other debris flow runout models have achieved when calibrated to the study area. For example, a runout model based on an empirical flow routing algorithm achieved a similarity index of 0.25 when applied to the San Ysidro watershed Gorr et al. (2022) and physics-based models (i.e. RAMMS, FLO-2D, D-CLAW) with various rheological assumptions had similarity indices between 0.23 and 0.26 Barnhart et al. (2021). Here, the similarity index is generally greater when the volume of sediment eroded from the upper watersheds is closer to

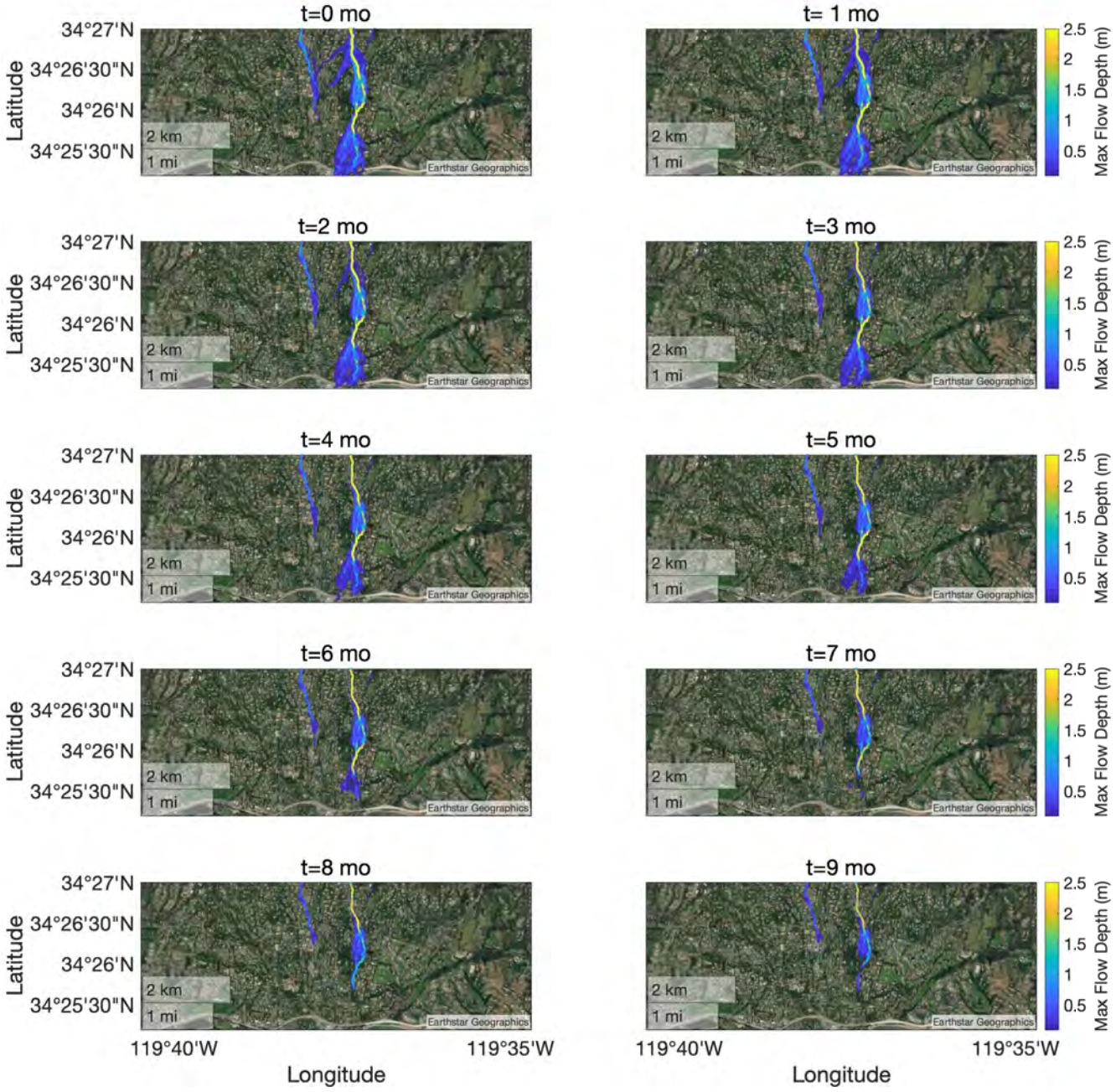

Figure 6. Maximum flow depth for several values of the hydraulic roughness coefficient and saturated hydraulic conductivity along with the corresponding time since fire from Figures 7b and 7c of Liu et al. 2021, respectively. All of the other parameters are set to the center value of their range. For contrast, the maximum color bar limit is set to 2.5 m although in the channels towards the north, maximum flow depth exceeds 2.5 m.

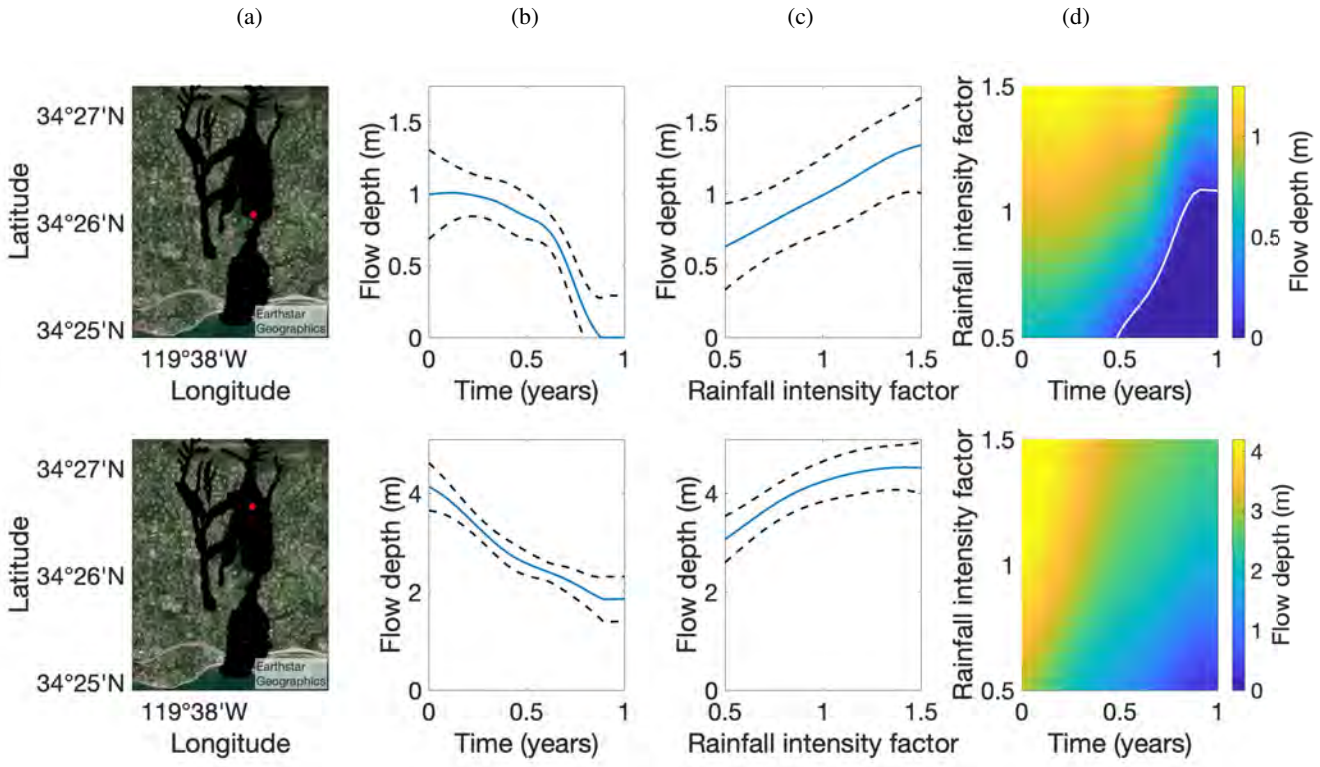

Figure 7. Exploration at one location on the fan (top row) and one location in the channel (bottom row). Panels in column (a) indicate locations of all emulated flow depths (black) and those being explored in detail (red). Panels in column (b) show peak flow depth as a function of time since fire. The hydraulic roughness coefficient and saturated hydraulic conductivity are parameterized as a function of time since fire Liu et al. (2021) while all other parameters set at their central values. (Note that the vertical scales are different; the maximum flow depth on the fan is roughly 1 m, and that in the channel is roughly 4 m.) Panels in column (c) show peak flow depth versus rainfall intensity with the hydraulic roughness coefficient and saturated hydraulic conductivity set to their respectively minimum values, which could be interpreted as a worst-case scenario immediately after a fire, and all other parameters set at their central values. Panels in column (d) contain color maps for maximum flow depth at these two locations varying all combinations of rainfall intensity and time since fire, which determines the hydraulic roughness coefficient and saturated hydraulic conductivity Liu et al. (2021). The white contours indicate the values of time since fire and rainfall intensity leading to a peak flow depth of 10 cm or more at the selected points.

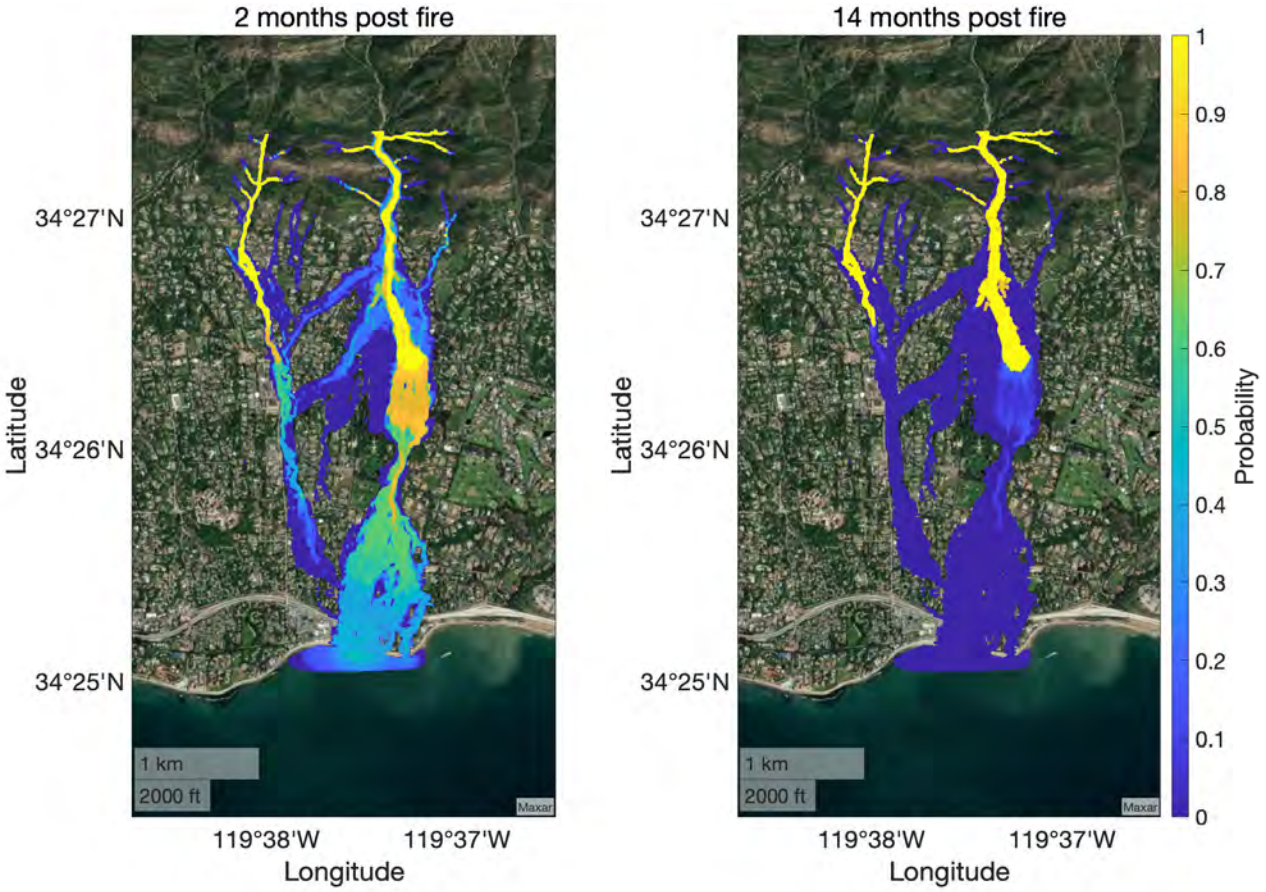

Figure 8. Probability of inundation maps, where a location is considered inundated if the maximum flow depth exceeds 10 cm. To calculate this probability, all parameters except the Manning coefficient and saturated hydraulic conductivity are set to their central values with the latter set to values corresponding to the 2 month and 14 month estimates from Liu et al. 2021, respectively.

the observed volume eroded. This observation is consistent with flow volume being an influential factor in debris flow runout, including specifically in our study area Barnhart et al. (2021).

Although the Titan2D model is able to reproduce both the observed sediment volume eroded from the upper watershed and the inundation pattern on the fan, the spatial patterns of erosion are not consistent with observations of widespread incision in higher order channels Morell et al. (2021) (Figure S3). Modeled erosion patterns are characterized by incision on hillslopes in areas of concentrated flow and in low order channels, which was also observed after the debris flow event Alessio et al. (2021). We attribute the limited amount of modeled erosion in high order channels, in part, to model assumptions and limitations. For example, since there is no established and generally applicable methodology for quantifying sediment entrainment rates by debris flow, the model neglects sediment entrainment when the volumetric sediment concentration exceeds 0.4 McGuire et al.

(2016, 2017). As a result, intense erosion that leads to high sediment concentrations and debris flow initiation in low order channels could result in higher order channels acting as transport zones for the debris flows that developed at lower drainage areas. We accept this limitation since our main objective is to simulate the downstream effects of debris flows rather than their growth rates or erosion patterns. Improved representation of sediment entrainment processes, particularly in channels and in portions of flow with sediment concentrations approaching those associated with debris flows, would be beneficial for future applications.

5.2 Model Sensitivity

Fire effects on soil and vegetation properties that affect the initiation and growth of runoff-generated debris flows are most extreme in the first few months following fire DeGraff et al. (2015); Thomas et al. (2021). Potentially rapid changes in hydrologic conditions following fire limit the time window for gathering data needed to constrain parameters for postfire runoff and erosion models, including the model used here. Aside from rainfall intensity, which will not be affected by the fire, we found that hydraulic roughness, the representative grain size, the fraction of stream power effective in sediment entrainment, and saturated hydraulic conductivity played the most important roles in controlling peak debris flow depth. Additional model testing across fire-prone regions in different geologic and climate settings is needed to assess model performance and determine the extent to which results related to parameter sensitivity are generalizable. Nonetheless, this result provides observational targets that can help focus future efforts to collect perishable postfire data.

Peak flow depth was most senstive to hydraulic roughness. We hypothesize that hydraulic roughness plays an important role in controlling inundated area and peak flow depths because of its influence on both modeled sediment detachment rates and flow resistance. Lower values of hydraulic roughness are associated with increased erosion from the upper watersheds (Figure S2). Saturated hydraulic conductivity will influence the rate at which sediment is detached by overland flow since it plays a role in controlling runoff magnitude and stream power. Increased rates of sediment detachment lead to increases in flow volume, which in turn act to increase runout and inundation potential Barnhart et al. (2021). Grain size, which is the second most influential parameter, similarly influences flow volume since a larger grain size will encourage more rapid deposition of sediment. The volume of sediment eroded from the upper watersheds decreases with δ (Figure S2).

Our evaluation of parameter sensitivity indicates that constraints on postfire values for hydraulic roughness, saturated hydraulic conductivity, fraction of stream power effective in sediment entrainment, and the grain size distribution of sediment entrained in debris flows would be beneficial for improving estimates of debris flow runout estimates. Burn severity is likely to play a substantial role in a fire's initial effect on these variables Moody et al. (2015); McGuire and Youberg (2020). In addition, attempts to capture changes in debris flow runout as a function of time since fire would benefit from methods to parameterize temporal changes in these influential parameters. Fire-driven reductions in hydraulic roughness are commonly cited as a cause for increased runoff and erosion McGuire and Youberg (2020); Stoof et al. (2015) as are increases in soil erodibility, which could be reflected in greater values of F, but there are few constraints on the temporal changes in hydraulic roughness or F following fire, which may be facilitated by changes in vegetation cover, ground cover, and/or grain roughness.

Particularly in southern California Doehring (1968); Florsheim et al. (1991); DiBiase and Lamb (2020) and other tectonically active regions in the western USA Roering and Gerber (2005), fire can promote substantial increases in dry ravel activity on hillslopes that can reduce hydraulic roughness by increasing the availability of fine sediment in channels. Hydraulic roughness may then increase over time as dry ravel deposits are progressively eroded during postfire rainstorms Tang et al. (2019). Temporal changes in debris flow sediment source locations Guilinger et al. (2020) and coarsening of particle size distributions due to preferential erosion of fines would also influence the effective grain size in the model. In practice, it is not clear how to quantitatively connect this single grain size parameter to the particle size distribution of hillslope or channel sediment, especially when flows contain boulders. Postfire changes in saturated hydraulic conductivity can be inferred from calibration of hydrologic models Liu et al. (2021), rainfall simulator experiments at the small plot scale Robichaud et al. (2016), and point scale measurements Ebel (2020); Ebel et al. (2022); Perkins et al. (2022). While some general patterns have been observed between time since fire and values of saturated hydraulic conductivity, there is substantial site-to-site variability Ebel and Martin (2017). The level of uncertainty in influential model input parameters and how they change over time highlights the need for probabilistic assessments of debris flow runout, which emulators can help to achieve by facilitating rapid exploration of large parameter spaces.

5.3 Debris flow hazards

Rainfall is a necessary driver for debris flow initiation and the model was also sensitive to rainfall intensity, specifically a rainfall intensity factor which we used to scale an observed rainfall intensity time series. This finding is consistent with observations that postfire basin-scale sediment yields Pak and Lee (2008) and debris flow volume Gartner et al. (2014); Gorr et al. (2024) increase with rainfall intensity averaged over durations of 60 minutes or less. Short duration (sub-hourly) bursts of high intensity rainfall are effective at generating infiltration-excess overland flow that can trigger debris flows in recently burned steeplands Kean et al. (2011); Nyman et al. (2011); Esposito et al. (2023). Emulators can be useful for generating probabilistic maps of debris flow inundation in response to design storms with different rainfall intensities or examining changes at particular points of interest. In cases where there are specific values at risk downstream of a burned area, rapid exploration of debris flow characteristics (i.e. peak flow depth) as a function of rainfall intensity could help define impact-based rainfall thresholds that could be used for planning and warning purposes. In other words, one could take advantage of the emulator's computational efficiency to determine not only the rainfall intensity required to initiate a debris flow, but also the rainfall intensity required to produce a debris flow that would impact a prescribed area of interest with some prescribed depth of flow. Such estimates could be particularly useful for assessing building damage Barnhart et al. (2024).

The computational cost of many physically-based debris flow models is a limitation in applications that are time sensitive, such as rapid postfire hazard assessments. Postfire debris flows in the western USA, such as those that occurred near Montecito, may occur before the fire has been officially contained and within weeks or months of fire ignition. Approximately 23% of postfire debris flow events, for example, initiate in the first 60 days following fire McGuire et al. (2024). The emulator methodology presented here provides one avenue for minimizing computation times, since an initial suite of simulations can be used to train the emulator which can later be applied with substantially less computational effort to generate a probabilistic

hazard map for a specific scenario. An emulator could even be trained prior to a fire. Analogous approaches have been employed in related applications Rutarindwa et al. (2019); Spiller et al. (2020). Within the context of postfire hazards, an emulator could be used to assess debris-flow runout and inundation downstream of a burned area in response to a design or forecast rainstorm. Atmospheric model ensembles, for example, can provide estimates of peak 15-minute rainfall intensity over watersheds of interest that could be used to constrain a distribution of rainfall intensity factors Oakley et al. (2023).

We focus on applications of surrogate modeling for postfire runoff-generated debris flows since accelerating MC calculations could be particularly beneficial within the context of rapid hazard assessments after fire when there are time constraints. However, the methodology presented here could similarly be applied to debris flows in unburned settings as well as to a broader range of geophysical flows. Runoff-generated debris flows, for example, can initiate in unburned alpine environments through processes that are similar to those that operate in recently burned watersheds Coe et al. (2008); Tang et al. (2020); Gregoretti and Fontana (2008); Bennett et al. (2014).

6 Conclusions

We applied a computationally expensive physics-based morphodynamic model and cost effective surrogates based on Gaussian process models to simulate postfire debris flows. We employ a Gaussian Process surrogate model, or emulator, to approximate peak flow depth from a physics-based morphodynamic model, Titan2D. The emulator is able to approximate the peak flow depth with a mean squared error that is generally in the range of $0.1 - 0.2$ m when using a modest training data set built from 64 Titan2D simulations. By parameterizing postfire changes in hydraulic roughness and saturated hydraulic conductivity, we demonstrate that the area inundated by postfire flows decreases substantially over a time period as short as 9 months. In many instances, the temporal persistence of debris flow hazards after fire is assessed through changes in the rainfall intensity required to intiate debris flows. Here here we illustrate the utility of cost-effective surrogates for extending this type of analysis to include information about how flow runout changes with time since fire. The range parameters associated with the emulator provide a metric for the relative importance of input parameters, which provides guidance for those that are most important to constrain for forward modeling of debris flow runout. We find that peak flow depths are most sensitive to changes in hydraulic roughness and grain size, while slightly less sensitive to a parameter related to sediment entrainment, a rainfall intensity factor, and saturated hydraulic conductivity. We highlight the emulator's ability to provide rapid estimates of peak flow depth for parameter combinations that were not part of the training data set by generating probabilistic maps of inundation as a function of time since fire. Emulator-based analyses can also facilitate rapid Monte Carlo calculations of inundation probability, making them a promising option for rapid postfire hazard assessments and scenario planning before a fire starts.

Code and data availability. The debris flow model under consideration in this paper is from McGuire et al. 2017 and it is accelerated by implementation in the Titan2D platform Patra et al. (2005); Simakov et al. (2019). Parametric models of the Manning coefficient and saturated

hydraulic conductivity versus time are available from Liu et al. 2021 as are validated samples of those same parameters for debris flows 2 and 14 months after fire. Packages to implement the parallel partial emulator Gu and Berger (2016) are available in Gu et al. 2019.

Author contributions. PP adapted the model code with assistance from LAM, AP, and EBP. PP performed the Titan2D simulations. LAM prepared the study site information and oversaw the geomorphology aspects of the project. ETS devised the surrogate models and oversaw the uncertainty quantification studies. ETS and LAM prepared the manuscript with contributions from all co-authors.

Competing interests. "The authors declare that they have no conflict of interest.

Acknowledgements. Spiller was supported by the National Science Foundation grant DMS-2053872 and Marquette University's Way Klingler Fellowship. McGuire was supported through the California Department of Water Resources Atmospheric River Program (4600013361). Patra and Patel were supported by the National Science Foundation grant OAC-2004302. Pitman was supported by the National Science Foundation grant DMS-2053874.

References

Alessio, P., Dunne, T., and Morell, K. (2021). Post-wildfire generation of debris-flow slurry by rill erosion on colluvial hillslopes. *Journal of Geophysical Research: Earth Surface*, 126(11):e2021JF006108.

Barnhart, K. R., Jones, R. P., George, D. L., McArdell, B. W., Rengers, F. K., Staley, D. M., and Kean, J. W. (2021). Multi-model comparison of computed debris flow runout for the 9 january 2018 montecito, california post-wildfire event. *Journal of Geophysical Research: Earth Surface*, 126(12):e2021JF006245.

Barnhart, K. R., Miller, C. R., Rengers, F. K., and Kean, J. W. (2024). Evaluation of debris-flow building damage forecasts. *Natural Hazards and Earth System Sciences*, 24(4):1459–1483.

Bayarri, M. J., Berger, J. O., Calder, E. S., Dalbey, K., Lunagómez, S., Patra, A. K., Pitman, E. B., Spiller, E. T., and Wolpert, R. L. (2009). Using statistical and computer models to quantify volcanic hazards. *Technometrics*, 51(4):402–413.

Bayarri, M. J., Berger, J. O., Calder, E. S., Patra, A. K., Pitman, E. B., Spiller, E. T., and Wolpert, R. L. (2015). A methodology for quantifying volcanic hazards. *International Journal of Uncertainty Quantification*, 5(4):297–325.

Bennett, G., Molnar, P., McArdell, B., and Burlando, P. (2014). A probabilistic sediment cascade model of sediment transfer in the illgraben. *Water Resources Research*, 50(2):1225–1244.

Coe, J. A., Kinner, D. A., and Godt, J. W. (2008). Initiation conditions for debris flows generated by runoff at chalk cliffs, central colorado. *Geomorphology*, 96(3-4):270–297.

Conedera, M., Peter, L., Marxer, P., Forster, F., Rickenmann, D., and Re, L. (2003). Consequences of forest fires on the hydrogeological response of mountain catchments: a case study of the riale buffaga, ticino, switzerland. *Earth Surface Processes and Landforms: The Journal of the British Geomorphological Research Group*, 28(2):117–129.

Currin, C., Mitchell, T., Morris, M., and Ylvisaker, D. (1988). A Bayesian approach to the design and analysis of computer experiments. Technical report, Oak Ridge National Laboratory, Oak Ridge, TN (USA).

Dalbey, K., Patra, A. ., Pitman, E. B., Bursik, M. I., and Sheridan, M. F. (2008). Input uncertainty propagation methods and hazard mapping of geophysical mass flows. *Journal of Geophysical Research: Solid Earth*, 113(B5):1–16.

DeGraff, J. V., Cannon, S. H., and Gartner, J. E. (2015). The timing of susceptibility to post-fire debris flows in the western united states. *Environmental & Engineering Geoscience*, 21(4):277–292.

Diakakis, M., Mavroulis, S., Vassilakis, E., and Chalvatzi, V. (2023). Exploring the application of a debris flow likelihood regression model in mediterranean post-fire environments, using field observations-based validation. *Land*, 12(3):555.

DiBiase, R. A. and Lamb, M. P. (2020). Dry sediment loading of headwater channels fuels post-wildfire debris flows in bedrock landscapes. *Geology*, 48(2):189–193.

Doehring, D. O. (1968). The effect of fire on geomorphic processes in the san gabriel mountains, california. *Rocky Mountain Geology*, 7(1):43–65.

Ebel, B. A. (2019). Measurement method has a larger impact than spatial scale for plot-scale field-saturated hydraulic conductivity (kfs) after wildfire and prescribed fire in forests. *Earth Surface Processes and Landforms*, 44(10):1945–1956.

Ebel, B. A. (2020). Temporal evolution of measured and simulated infiltration following wildfire in the colorado front range, usa: Shifting thresholds of runoff generation and hydrologic hazards. *Journal of Hydrology*, 585:124765.

Ebel, B. A. and Martin, D. A. (2017). Meta-analysis of field-saturated hydraulic conductivity recovery following wildland fire: Applications for hydrologic model parameterization and resilience assessment. *Hydrological Processes*, 31(21):3682–3696.

Ebel, B. A., Moody, J. A., and Martin, D. A. (2022). Post-fire temporal trends in soil-physical and-hydraulic properties and simulated runoff generation: Insights from different burn severities in the 2013 black forest fire, co, usa. *Science of the Total Environment*, 802:149847.

Esposito, G., Gariano, S. L., Masi, R., Alfano, S., and Giannatiempo, G. (2023). Rainfall conditions leading to runoff-initiated post-fire debris flows in campania, southern italy. *Geomorphology*, 423:108557.

Florsheim, J. L., Keller, E. A., and Best, D. W. (1991). Fluvial sediment transport in response to moderate storm flows following chaparral wildfire, ventura county, southern california. *Geological Society of America Bulletin*, 103(4):504–511.

Gabet, E. J. and Bookter, A. (2008). A morphometric analysis of gullies scoured by post-fire progressively bulked debris flows in southwest montana, usa. *Geomorphology*, 96(3-4):298–309.

Gartner, J. E., Cannon, S. H., and Santi, P. M. (2014). Empirical models for predicting volumes of sediment deposited by debris flows and sediment-laden floods in the transverse ranges of southern california. *Engineering Geology*, 176:45–56.

Gibson, S., Moura, L. Z., Ackerman, C., Ortman, N., Amorim, R., Floyd, I., Eom, M., Creech, C., and Sánchez, A. (2022). Prototype scale evaluation of non-newtonian algorithms in hec-ras: Mud and debris flow case studies of santa barbara and brumadinho. *Geosciences*, 12(3):134.

Gorr, A. N., McGuire, L. A., and Youberg, A. M. (2024). Empirical models for postfire debris-flow volume in the southwest united states. *Journal of Geophysical Research: Earth Surface*, 129(11):e2024JF007825.

Gorr, A. N., McGuire, L. A., Youberg, A. M., and Rengers, F. K. (2022). A progressive flow-routing model for rapid assessment of debris-flow inundation. *Landslides*, 19(9):2055–2073.

Graber, A. P., Thomas, M. A., and Kean, J. W. (2023). How long do runoff-generated debris-flow hazards persist after wildfire? *Geophysical Research Letters*, 50(19):e2023GL105101.

Gregoretti, C. and Fontana, G. D. (2008). The triggering of debris flow due to channel-bed failure in some alpine headwater basins of the dolomites: Analyses of critical runoff. *Hydrological Processes: An International Journal*, 22(13):2248–2263.

Gu, M. and Berger, J. O. (2016). Parallel partial Gaussian process emulation for computer models with massive output. *The Annals of Applied Statistics*, 10(3):1317–1347.

Gu, M., Palomo, J., and Berger, J. O. (2019). RobustGaSP: Robust Gaussian Stochastic Process Emulation in R. *The R Journal*, 11(1):112–136.

Gu, M., Wang, X., and Berger, J. O. (2018). Robust gaussian stochastic process emulation. *The Annals of Statistics*, 46(6A):3038–3066.

Guilinger, J. J., Gray, A. B., Barth, N. C., and Fong, B. T. (2020). The evolution of sediment sources over a sequence of postfire sediment-laden flows revealed through repeat high-resolution change detection. *Journal of Geophysical Research: Earth Surface*, 125(10):e2020JF005527.

Hairsine, P. and Rose, C. (1992a). Modeling water erosion due to overland flow using physical principles: 1. sheet flow. *Water resources research*, 28(1):237–243.

Hairsine, P. and Rose, C. (1992b). Modeling water erosion due to overland flow using physical principles: 2. rill flow. *Water resources research*, 28(1):245–250.

Heiser, M., Scheidl, C., and Kaitna, R. (2017). Evaluation concepts to compare observed and simulated deposition areas of mass movements. *Computational Geosciences*, 21:335–343.

Hoch, O. J., McGuire, L. A., Youberg, A. M., and Rengers, F. K. (2021). Hydrogeomorphic recovery and temporal changes in rainfall thresholds for debris flows following wildfire. *Journal of Geophysical Research: Earth Surface*, 126(12):e2021JF006374.

Iverson, R. M., Reid, M. E., and LaHusen, R. G. (1997). Debris-flow mobilization from landslides. *Annual Review of Earth and Planetary Sciences*, 25(1):85–138.

Jakob, M., Hungr, O., and Pierson, T. C. (2005). Hyperconcentrated flow—transitional process between water flow and debris flow. *Debris-flow hazards and related phenomena*, pages 159–202.

Kean, J. W., Staley, D. M., and Cannon, S. H. (2011). In situ measurements of post-fire debris flows in southern california: Comparisons of the timing and magnitude of 24 debris-flow events with rainfall and soil moisture conditions. *Journal of Geophysical Research: Earth Surface*, 116(F4).

Kean, J. W., Staley, D. M., Lancaster, J. T., Rengers, F. K., Swanson, B. J., Coe, J. A., Hernandez, J., Sigman, A., Allstadt, K. E., and Lindsay, D. N. (2019). Inundation, flow dynamics, and damage in the 9 january 2018 montecito debris-flow event, california, usa: Opportunities and challenges for post-wildfire risk assessment. *Geosphere*, 15(4):1140–1163.

Kinnell, P. (2005). Raindrop-impact-induced erosion processes and prediction: a review. *Hydrological Processes: An International Journal*, 19(14):2815–2844.

Lamb, M. P., Scheingross, J. S., Amidon, W. H., Swanson, E., and Limaye, A. (2011). A model for fire-induced sediment yield by dry ravel in steep landscapes. *Journal of Geophysical Research: Earth Surface*, 116(F3).

Lancaster, J. T., Swanson, B. J., Lukashov, S. G., Oakley, N. S., Lee, J. B., Spangler, E. R., Hernandez, J. L., Olson, B. P., DeFrisco, M. J., Lindsay, D. N., et al. (2021). Observations and analyses of the 9 january 2018 debris-flow disaster, santa barbara county, california. *Environmental & Engineering Geoscience*, 27(1):3–27.

Liu, T., McGuire, L. A., Wei, H., Rengers, F. K., Gupta, H., Ji, L., and Goodrich, D. C. (2021). The timing and magnitude of changes to hortonian overland flow at the watershed scale during the post-fire recovery process. *Hydrological Processes*, 35(5):e14208.

McGuire, L. A., Ebel, B. A., Rengers, F. K., Vieira, D. C., and Nyman, P. (2024). Fire effects on geomorphic processes. *Nature Reviews Earth & Environment*, pages 1–18.

McGuire, L. A., Kean, J. W., Staley, D. M., Rengers, F. K., and Wasklewicz, T. A. (2016). Constraining the relative importance of raindrop- and flow-driven sediment transport mechanisms in postwildfire environments and implications for recovery time scales. *Journal of Geophysical Research: Earth Surface*, 121(11):2211–2237.

McGuire, L. A., Rengers, F. K., Kean, J. W., and Staley, D. M. (2017). Debris flow initiation by runoff in a recently burned basin: Is grain-by-grain sediment bulking or en masse failure to blame? *Geophysical Research Letters*, 44(14):7310–7319.

McGuire, L. A., Rengers, F. K., Oakley, N., Kean, J. W., Staley, D. M., Tang, H., de Orla-Barile, M., and Youberg, A. M. (2021). Time since burning and rainfall characteristics impact post-fire debris-flow initiation and magnitude. *Environmental & Engineering Geoscience*, 27(1):43–56.

McGuire, L. A. and Youberg, A. M. (2020). What drives spatial variability in rainfall intensity-duration thresholds for post-wildfire debris flows? insights from the 2018 buzzard fire, nm, usa. *Landslides*, 17(10):2385–2399.

McKay, M. D., Beckman, R. J., and Conover, W. J. (1979). A comparison of three methods for selecting values of input variables in the analysis of output from a computer code. *Technometrics*, 21(2):239–245.

Moody, J. A., Ebel, B. A., Nyman, P., Martin, D. A., Stoof, C., and McKinley, R. (2015). Relations between soil hydraulic properties and burn severity. *International Journal of Wildland Fire*, 25(3):279–293.

Moody, J. A., Shakesby, R. A., Robichaud, P. R., Cannon, S. H., and Martin, D. A. (2013). Current research issues related to post-wildfire runoff and erosion processes. *Earth-Science Reviews*, 122:10–37.

Morell, K., Alessio, P., Dunne, T., and Keller, E. (2021). Sediment recruitment and redistribution in mountain channel networks by post-wildfire debris flows. *Geophysical Research Letters*, 48(24):e2021GL095549.

Nyman, P., Sheridan, G. J., Smith, H. G., and Lane, P. N. (2011). Evidence of debris flow occurrence after wildfire in upland catchments of south-east australia. *Geomorphology*, 125(3):383–401.

Nyman, P., Smith, H. G., Sherwin, C. B., Langhans, C., Lane, P. N., and Sheridan, G. J. (2015). Predicting sediment delivery from debris flows after wildfire. *Geomorphology*, 250:173–186.

Oakley, N. S., Cannon, F., Munroe, R., Lancaster, J. T., Gomberg, D., and Ralph, F. M. (2018). Brief communication: Meteorological and climatological conditions associated with the 9 january 2018 post-fire debris flows in montecito and carpinteria, california, usa. *Natural Hazards and Earth System Sciences*, 18(11):3037–3043.

Oakley, N. S., Liu, T., McGuire, L. A., Simpson, M., Hatchett, B. J., Tardy, A., Kean, J. W., Castellano, C., Laber, J. L., and Steinhoff, D. (2023). Toward probabilistic post-fire debris-flow hazard decision support. *Bulletin of the American Meteorological Society*.

Orem, C. A. and Pelletier, J. D. (2016). The predominance of post-wildfire erosion in the long-term denudation of the valles caldera, new mexico. *Journal of Geophysical Research: Earth Surface*, 121(5):843–864.

Pak, J. H. and Lee, J.-J. (2008). A statistical sediment yield prediction model incorporating the effect of fires and subsequent storm events 1. *JAWRA Journal of the American Water Resources Association*, 44(3):689–699.

Patra, A. K., Bauer, A. C., Nichita, C., Pitman, E. B., Sheridan, M. F., Bursik, M., Rupp, B., Webb, A., Namikawa, L., and Renschler, C. (2005). Parallel adaptive numerical simulation of dry avalanches over natural terrain. *Journal of Volcanology and Geothermal Research*, 139:1–21. doi:10.1016/j.jvolgeores.2004.06.014; available online Oct, 2004.

Perkins, J. P., Diaz, C., Corbett, S. C., Cerovski-Darriau, C., Stock, J. D., Prancevic, J. P., Micheli, E., and Jasperse, J. (2022). Multi-stage soil-hydraulic recovery and limited ravel accumulations following the 2017 nuns and tubbs wildfires in northern california. *Journal of Geophysical Research: Earth Surface*, 127(6):e2022JF006591.

Pierson, T. C. and Costa, J. E. (1987). A rheologic classification of subaerial sediment-water flows. *Reviews in engineering geology*, 7:1–12.

Rasmussen, C. E. and Williams, C. K. I. (2006). *Gaussian Processes for Machine Learning*. Adaptative computation and machine learning series. The MIT Press, Boston, MA.

Rengers, F. K., McGuire, L. A., Kean, J. W., Staley, D. M., and Hobley, D. (2016). Model simulations of flood and debris flow timing in steep catchments after wildfire. *Water Resources Research*, 52(8):6041–6061.

Robichaud, P. R., Wagenbrenner, J. W., Pierson, F. B., Spaeth, K. E., Ashmun, L. E., and Moffet, C. A. (2016). Infiltration and interrill erosion rates after a wildfire in western montana, usa. *Catena*, 142:77–88.

Roering, J. J. and Gerber, M. (2005). Fire and the evolution of steep, soil-mantled landscapes. *Geology*, 33(5):349–352.

Rutarindwa, R., Spiller, E. T., Bevilacqua, A., Bursik, M. I., and Patra, A. K. (2019). Dynamic probabilistic hazard mapping in the Long Valley Volcanic Region, CA: Integrating vent opening maps and statistical surrogates of physical models of pyroclastic density currents. *Journal of Geophysical Research: Solid Earth*, 124(9):9600–9621.

Sacks, J., Schiller, S. B., and Welch, W. J. (1989a). Designs for computer experiments. *Technometrics*, 31(1):41–47.

Sacks, J., Welch, W. J., Mitchell, T. J., and Wynn, H. P. (1989b). Design and analysis of computer experiments. *Statistical Science*, 4(4):409–423.

Santi, P. M., dewolfe, V. G., Higgins, J. D., Cannon, S. H., and Gartner, J. E. (2008). Sources of debris flow material in burned areas. *Geomorphology*, 96(3-4):310–321.

Santner, T. J., Williams, B. J., and Notz, W. I. (2003). *The Design and Analysis of Computer Experiments*. Springer Series in Statistics. Springer-Verlag, New York, NY.

Sheridan, G. J., Lane, P. N., and Noske, P. J. (2007). Quantification of hillslope runoff and erosion processes before and after wildfire in a wet eucalyptus forest. *Journal of Hydrology*, 343(1-2):12–28.

Simakov, N. A., Jones-Ivey, R. L., Akhavan-Safaei, A., Aghakhani, H., Jones, M. D., and Patra, A. K. (2019). Modernizing titan2d, a parallel amr geophysical flow code to support multiple rheologies and extendability. In *International Conference on High Performance Computing*, pages 101–112. Springer.

Spiller, E. T., Bayarri, M. J., Berger, J. O., Calder, E. S., Patra, A. K., Pitman, E. B., and Wolpert, R. L. (2014). Automating emulator construction for geophysical hazard maps. *SIAM/ASA Journal of Uncertainty Quantification*, 2(1):126–152.

Spiller, E. T., Wolpert, R. L., Ogburn, S. E., Calder, E. S., Berger, J. O., Patra, A. K., and Pitman, E. B. (2020). Volcanic hazard assessment for an eruption hiatus, or post-eruption unrest context: Modeling continued dome collapse hazards for Soufrière Hills Volcano. *Frontiers in Earth Science: Geohazards and Georisks*, 8(535567):396.

Spiller, E. T., Wolpert, R. L., Tierz, P., and Asher, T. G. (2023). The zero problem: Gaussian process emulators for range-constrained computer models. *SIAM/ASA Journal on Uncertainty Quantification*, 11(2):540–566.

Staley, D. M., Negri, J. A., Kean, J. W., Laber, J. L., Tillery, A. C., and Youberg, A. M. (2017). Prediction of spatially explicit rainfall intensity–duration thresholds for post-fire debris-flow generation in the western united states. *Geomorphology*, 278:149–162.

Staley, D. M., Wasklewicz, T. A., and Kean, J. W. (2014). Characterizing the primary material sources and dominant erosional processes for post-fire debris-flow initiation in a headwater basin using multi-temporal terrestrial laser scanning data. *Geomorphology*, 214:324–338.

Stefanescu, E. R., Bursik, M., Cordoba, G., Dalbey, K., Jones, M. D., Patra, A. K., Pieri, D. C., Pitman, E. B., and Sheridan, M. F. (2012a). Digital elevation model uncertainty and hazard analysis using a geophysical flow model. *Proceedings of the Royal Society A: Mathematical, Physical and Engineering Sciences*, 468(2142):1543–1563.

Stefanescu, E. R., Bursik, M., and Patra, A. K. (2012b). Effect of digital elevation model on mohr-coulomb geophysical flow model output. *Natural hazards*, 62(2):635–656.

Stein, M. L. (1999). *Interpolation of Spatial Data*.

Stoof, C. R., Ferreira, A. J., Mol, W., Van den Berg, J., De Kort, A., Drooger, S., Slingerland, E. C., Mansholt, A. U., Ferreira, C. S., and Ritsema, C. J. (2015). Soil surface changes increase runoff and erosion risk after a low–moderate severity fire. *Geoderma*, 239:58–67.

Stoof, C. R., Vervoort, R., Iwema, J., Van Den Elsen, E., Ferreira, A., and Ritsema, C. (2012). Hydrological response of a small catchment burned by experimental fire. *Hydrology and Earth System Sciences*, 16(2):267–285.

Struble, W. T., McGuire, L. A., McCoy, S. W., Barnhart, K. R., and Marc, O. (2023). Debris-flow process controls on steepland morphology in the san gabriel mountains, california. *Journal of Geophysical Research: Earth Surface*, 128(7):e2022JF007017.

Tang, H., McGuire, L. A., Kean, J. W., and Smith, J. B. (2020). The impact of sediment supply on the initiation and magnitude of runoff-generated debris flows. *Geophysical Research Letters*, 47(14):e2020GL087643.

Tang, H., McGuire, L. A., Rengers, F. K., Kean, J. W., Staley, D. M., and Smith, J. B. (2019). Evolution of debris-flow initiation mechanisms and sediment sources during a sequence of postwildfire rainstorms. *Journal of Geophysical Research: Earth Surface*, 124(6):1572–1595.

Thomas, M. A., Rengers, F. K., Kean, J. W., McGuire, L. A., Staley, D. M., Barnhart, K. R., and Ebel, B. A. (2021). Postwildfire soil-hydraulic recovery and the persistence of debris flow hazards. *Journal of Geophysical Research: Earth Surface*, 126(6):e2021JF006091.

Wagenbrenner, J., Robichaud, P., and Elliot, W. (2010). Rill erosion in natural and disturbed forests: 2. modeling approaches. *Water Resources Research*, 46(10).

Welch, W. J., Buck, R. J., Sacks, J., Wynn, H. P., Mitchell, T. J., and Morris, M. D. (1992). Screening, predicting, and computer experiments. *Technometrics*, 34(1):15–25.

Zhao, H., Amann, F., and Kowalski, J. (2021). Emulator-based global sensitivity analysis for flow-like landslide run-out models. *Landslides*, 18(10):3299–3314.

Zhao, H. and Kowalski, J. (2022). Bayesian active learning for parameter calibration of landslide run-out models. *Landslides*, pages 1–13.